Identification and tagging of double b-hadron jets from gluon splitting with the ATLAS Detector

Lic. María Laura González Silva

UNIVERSIDAD DE BUENOS AIRES

Facultad de Ciencias Exactas y Naturales

Departamento de Física

Identification and tagging of double b-hadron jets from gluon splitting with the ATLAS Detector

Trabajo de Tesis para optar por el título de
Doctor de la Universidad de Buenos Aires en el área Ciencias Físicas

por   **María Laura González Silva**

Director de Tesis: Dr. Ricardo Piegaia

Consejero de estudios: Dr. Daniel Deflorian

Lugar de Trabajo: Departamento de Física (CONICET-UBA)

Buenos Aires, 2012

AGRADECIMIENTOS

Quiero agradecer a mi director, Ricardo Piegaia, y a todos aquellos que trabajaron junto conmigo en el experimento ATLAS, Gastón Romeo, Gustavo Otero y Garzón, Hernán Reisin y Sabrina Sacerdotti. Un especial agradecimiento a Ariel Schwartzman y su equipo.

Quiero agradecer también a mis compañeros de grupo y oficina, Javier Tiffenberg, Yann Guardincerri, Pablo Pieroni y Orel Gueta.

Quiero agradecer al Experimento ATLAS, al programa HELEN y al programa e-Planet. Quiero agradecer al CONICET y a la Fundación Exactas por hacer posible la realización de esta tesis.

Quiero agradecer el apoyo de mis compañeros de la carrera, especialmente a mis amigos Cecilia Bejarano y Tomas Teitelbaum.

Quiero agradecer a los amigos que hice a lo largo de estos años en mis visitas al Laboratorio CERN, y a mis colegas y amigos de la Universidad de la Plata. Un especial agradecimiento a Fernando Monticelli.

Quiero agradecer a mis amigos de la vida por continuar a mi lado a pesar de las ausencias.

Finalmente, quiero agradecer a mi familia por su apoyo y comprensión, especialmente a Cristina Silva, Lorena González y Juan Martín Alba.

Abstract

Esta tesis describe un método que permite la identificación de jets que contienen dos hadrones b, que se originan en la división de un gluon en un par $b\bar{b}$. La técnica desarrollada explota las diferencias cinemáticas entre los llamados jets "merged" y los genuinos jets b, usando variables que describen la estructura interna y la forma de los jets, construidas a partir de las trazas asociadas a los mismos. Las variables con mayor poder discriminador son combinadas en un análisis de multivariable. Poder identificar y remover jets b que provienen de la división de un gluon es importante para la estimación y la redución del fondo a señales de física dentro del Modelo Estándar y en nueva física. El algoritmo diseñado rechaza, en eventos simulados, el 95% (50%) de los jets "merged", mientras que retiene el 50% (90%) de los jets b genuinos.

Palabras clave: Experimento ATLAS, Jets, Subestructura de Jets, Etiquetado de Jets b, *Gluon Splitting*.

Abstract

This thesis describes a method that allows the identification of double B-hadron jets originating from gluon-splitting. The technique exploits the kinematic differences between the so called "merged" jets and single B-hadron jets using track-based jet shape and jet substructure variables combined in a multivariate likelihood analysis. The ability to reject b-jets from gluon splitting is important to reduce and to improve the estimation of the b-tag background in Standard Model analyses and in new physics searches involving b-jets in the final state. In the simulation, the algorithm rejects 95% (50%) of merged B-hadron jets while retaining 50% (90%) of the tagged b-jets, although the exact values depend on the jet p_T.

Keywords: ATLAS Experiment, Jets, Jet Substructure, b-tagging, Gluon Splitting.

Contents

Chapter 1

Event reconstruction and b-Tagging

The event reconstruction software, which in ATLAS is implemented in the software framework ATHENA, process the events starting from the raw data obtained from the various sub-detectors (energy deposits and hits), processing them in many different stages and finally interpreting them as a set of charged tracks, electrons, photons, jets, muons and, in general, of possible kinds of final state objects with related four momenta. In this chapter the reconstruction of these objects is briefly described together with the algorithms for the identification of b-quark jets. These algorithms are mainly based on the reconstruction of the primary interaction vertex, on the reconstruction of charged particles in the Inner Detector and on the reconstruction of jets in the calorimeter.

1.1 Jet reconstruction and calibration

Hadronic jets used for ATLAS analyses are reconstructed by a jet algorithm, starting from the energy depositions of electromagnetic and hadronic showers in the calorimeters. Two different size parameters are used: $R = 0.4$, for narrow jets, and $R = 0.6$, for wider jets. The default jet algorithm is the anti-kt algorithm, described in the previous chapter. Due to the expected level of pile-up in the LHC, the primary factor that influenced the selection of this algorithm was the effect of multiple simultaneous interactions on the reconstruction of jets. The original ATLAS cone algorithm, known to contain infrared and collinear sensitivity, is highly susceptible to this effect. On the contrary, the anti-kt algorithm is the most stable after the introduction of pile-up [1].

The input to calorimeter jet reconstruction can be calorimeter towers or topological cell clusters. Charged particle tracks reconstructed in the Inner Detectors are also used to define jets. These constituents have the further advantage of being insensitive to pile-up and they provide a stable reference for systematic studies. The jet inputs are combined as massless four-momentum objects in order to form the final four-momentum of the jet, which allows for a well-defined jet mass [2]. In the case of track-jets, the track four-momentum is constructed assuming the π meson mass for each track.

Calorimeter towers are static, $\Delta\eta \times \Delta\phi = 0.1 \times 0.1$, grid elements built directly from calorimeter cells. There are two types of calorimeter towers: with or without noise supression. The latter are called "noise-suppressed" towers and use only the cells with energies above a certain noise threshold. The noise of a calorimeter cell is measured by recording calorimeter signals in periods where no beam is present in the acelerator. The standard deviation

3

σ around the mean measured energy is interpreted as the noise of the cell, and dependes on the sampling layer in which the cell resides and the position in η.

The results presented in this thesis show jets which were built from noise-suppressed topological clusters of energy in the calorimeter, aslo known as "topo-clusters" [3]. Topological clusters are groups of calorimeter cells that are designed to follow the shower development taking advantage of the fine segmentation of the ATLAS calorimeters. The topological cluster formation starts from a seed cell with $|E_{cell}| > 4\sigma$ above the noise. In a second step, neighbor cells that have an energy at least 2σ above their mean noise are added to the cluster. Finally, all nearest-neighbor cells surrounding the clustered cells are added to the cluster, regardless of signal-to-noise ratio[1]. The position of the cluster is assigned as the energy-weighted centroid of all constituent cells (the weight used is the absolute cell energy).

In Monte Carlo simulation, reference jets ("truth jets") are formed from simulated stable particles using the jet algorithm utilized for the reconstructed jets.

Jet calibration

The purpose of the jet energy calibration, or jet energy scale (JES), is to correct the measured electromagnetic scale (EM scale) energy to the energy of the stable particles within a jet. The jet energy calibration must account then for the calorimeter non-compensation; the energy lost in inactive regions of the detector, such as in the cryostat walls or cabling; energy that escapes the calorimeters, such as that of highly-energetic particles that "punch-through"

---

[1]Noise-supressed towers also make use of the topological clusters algorithm [3] to select cells, i.e. only calorimeter cells that are included in topo-clusters are used.

to the muon system; energy of cells that are not included in clusters, due to inefficiencies in the noise-suppression scheme; and energy of clusters not included in the final reconstructed jet, due to inefficiencies in the jet reconstruction algorithm. The muons and neutrinos that may be present within the jet are not expected to interact within the calorimeters, and are not included in this energy calibration. Due to the varying calorimeter coverage, detector technology, and amount of upstream inactive material, the calibration that must be applied to each jet to bring it to the hadronic scale varies with its η position within the detector.

The jet energy is first reconstructed from the constituent cell energies at EM scale. These cells have been calibrated to return the energy corresponding to electromagnetic showers in the calorimeter, based on test-beam injection of electrons and pions [4], measurements of cosmic muons [5] and the reconstruction of the Z mass peak in $Z \to ee$ decays [6]. The correction for the lower response to hadrons is based on the topology of the energy depositions observed in the calorimeter.

In the simplest case the measured jet energy is corrected, on average, using Monte Carlo simulations, as follows:

$$E_{calib}^{jet} = E_{meas}^{jet}/F_{calib}(E_{meas}^{jet}), \;\; \text{with } E_{meas}^{jet} = E_{EM}^{jet} - O(\text{NPV}), \qquad (1.1)$$

where E_{EM}^{jet} is the calorimeter energy measured at the electromagnetic scale, E_{calib}^{jet} is the calibrated energy and F_{calib} is the calibration function that depends on the measured jet energy and is evaluated in small jet η regions. The variable $O(\text{NPV})$ denotes the correction for additional energy from multiple proton-proton interactions depending on the number of primary vertices (NPV).

The simplest calibration scheme and the one used in this thesis is the so called "EM+JES". This calibration applies the corrections as a function of the

jet energy and pseudorapidity to jets reconstructed at the electromagnetic scale. The additional energy due to multiple proton-proton collisions within the same bunch crossing (pile-up) is corrected before the hadronic energy scale is restored, such that the derivation of the jet energy scale calibration is factorised and does not depend on the number of additional interactions in the event. The EM+JES calibration scheme consists of three subsequent steps:

- Pile-up correction: An offset correction is applied in order to substract the additional average energy measured in the calorimeter due to multiple proton-proton interactions. This correction is derived from minimum bias data as a function of NPV, the jet pseudorapidity and the bunch spacing.

- Vertex correction: The jet four momentum is corrected such that the jet originates from the primary vertex of the interaction instead of the geometrical centre of the detector.

- Jet energy and direction correction: The jet energy and direction are corrected using constants derived from the comparison of the kinematic observables of reconstructed jets and those from truth jets in the simulation.

In the final step the calibration is derived in terms of the energy response of the jet, or the ratio of the reconstructed jet energy to that of a truth jet. The EM scale response is written as,

$$R_{EM}^{jet} = E_{EM}^{jet}/E_{truth}^{jet} \tag{1.2}$$

To compute this quantity, reconstructed jets must be matched to isolated jets in the Monte Carlo within $\Delta R < 0.3$. The isolation requirement is

applied in order to factorize the effects due to close-by jets from those due to purely detector effects such as dead material and non-compensation. The isolation criterion requires that no other jet with a $p_T > 7$ GeV be within $\Delta R < 2.5R$, where R is the distance parameter of the jet algorithm. The EM scale energy response is binned in truth jet energy, E^{jet}_{truth}, and the calorimeter jet detector η. For each (E^{jet}_{truth}, η)-bin, the averaged jet response is defined as the peak position of a Gaussian fit to the $E^{jet}_{EM}/E^{jet}_{truth}$ distribution. A function $F_{calib,k}(E^{jet}_{EM})$ is then defined for each η-bin k that describes the response as a function of the uncalibrated jet energy. $F_{calib,k}(E^{jet}_{EM})$ is parameterised as:

$$F_{calib,k}(E^{jet}_{EM}) = \sum_{i=0}^{N_{max}} a_i (\ln E^{jet}_{EM})^i, \qquad (1.3)$$

where a_i are free parameters, and N_{max} is chosen between 1 and 6 depending on the goodness of the fit. The final jet energy scale correction that relates the measured calorimeter jet energy scale to the hadronic scale is then defined as $1/F_{calib,k}(E^{jet}_{EM})$ in the following:

$$E^{jet}_{EM+JES} = \frac{E^{jet}_{EM}}{F_{calib}(E^{jet}_{EM})|_\eta}, \qquad (1.4)$$

where $F_{calib}(E^{jet}_{EM})|_\eta$ is $F_{calib,k}(E^{jet}_{EM})$ for the relevant η-bin k.

Other calibrations schemes are the global calorimeter cell weighting (GCW) calibration and the local cluster weighting (LCW) calibration. The GCW scheme exploits the observation that electromagnetic showers in the calorimeter leave more compact energy depositions than hadronic showers with the same energy. Energy corrections are derived for each cell within a jet. The cell corrections account for all energy loses of a jet in the detector. Since these corrections are only applicable to jets and not to energy depositions, they are called "global" corrections.

The LCW calibration method first classifies topo-clusters as either electromagnetic of hadronic, based on the measured energy density. Energy

corrections are derived according to this classification from single charged and neutral pion Monte Carlo simulations. Dedicated corrections are derived for the effects of non-compensation, signal losses due to noise threshold effects, and energy lost in non-instrumented regions. Since the energy corrections are applied without reference to a jet definition they are called "local" corrections. Jets are then built from these calibrated clusters using a jet algorithm.

The final jet energy calibration can be applied to EM scale jets, with the resulting calibrated jets referred to as EM+JES, or to LCW (GCW) calibrated jets, with the resulting jets referred to as LCW+JES (GCW+JES) jets.

A further jet calibration scheme called global sequential (GS) calibration, starts from jets calibrated with the EM+JES calibration and exploits the topology of the energy deposits in the calorimeter to characterise fluctuations in the jet particle content of the hadronic shower development. Correcting for such fluctuations can improve the jet energy resolution. The correction uses several jet properties, and each correction is applied sequentially.

For the 2011 data the recomended calibration schemes were the EM+JES and the LCW calibrations. The simple EM+JES calibration does not provide the best performance, but allows in the central detector region the most direct evaluation of the systematic uncertainties from the calorimeter response to single isolated hadrons measured *in situ* and in test-beams and from systematic variations in the Monte Carlo simulation. For the LCW+JES calibration scheme the JES uncertainty is determined from *in situ* techniques. For all calibration schemes, the JES uncertainty in the forward regions is derived from the uncertainty in the central region using the transverse momentum balance in events where only two jets are produced.

Jet energy scale uncertainties for the EM+JES scheme

For many physics analyses, the uncertainty on the JES constitutes the dominant systematic uncertainty because of its tendency to shift jets in and out of analysis selections due to the steeply falling jet p_T spectrum. The uncertainty on the EM+JES scale is determined primarily by six factors: varying the physics models for hadronization and parameters of the Monte Carlo generators, evaluating the baseline calorimeter response to single particles, comparing multiple models for the detector simulation of hadronic showers, assesing the calibration scales as a function of pseudorapidity, and by adjusting the JES calibration methods itself. The final JES uncertainty in the central region, $|\eta| < 0.8$, is determined from the maximum deviation in response observed with respect to the response in the nominal sample. For the more forward region, the so called "η-intercalibration" contribution is estimated. This is a procedure that uses direct di-jet balance measurements in two-jet events to measure the relative energy scale of jets in the more forward regions compared to jets in a reference region. The technique exploits the fact that these jets are expected to have equal p_T due to transverse momentum conservation. Figure 1.1 shows the final fractional jet energy scale uncertainty and its individual contributions as a function of p_T for a central η region. The JES uncertainty for anti-kt jets with $R = 0.4$ is between $\approx$4% (8%, 14%) at low jet p_T and $\approx$2.5%-3% (2.5%-3.5%, 5%) for jets with $p_T > 60$ GeV in the central (endcap, forward) region.

In addition to the tests above, *in situ* tests of the JES using direct γ-jet balance, multi-jet balance, and track-jets indicate that the uncertainties in Fig. 1.1 reflect accurately the true uncertainties in the JES.

In the case of jets induced by bottom quarks (*b*-jets), the calorimeter response uncertainties are also evaluated using single hadron response mea-
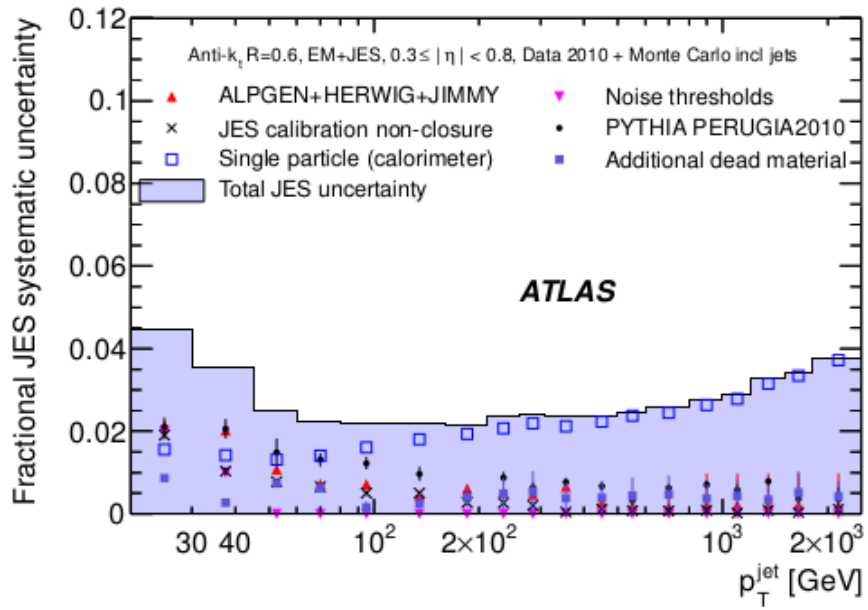
Figure 1.1: Fractional jet energy scale uncertainty as a function of jet p_T for jets in the pseudorapidity region $0.3 < |\eta| < 0.8$ in the calorimeter barrel. The total uncertainty is shown as the solid tight blue area. The individual sources are also shown.

surements *in situ* and in test beams [7]. For jets within $|\eta| < 0.8$ and $20 \leq p_T < 250$ GeV the expected difference in the calorimeter response uncertainty of identified b-jets with respect to the one of inclusive jets is less than 0.5%. It is assumed that this uncertainty extends up to $|\eta| < 2.5$.

The JES uncertainty arising from the modelling of the b-quark fragmentation can be determined from systematics variations of the Monte Carlo simulation. The fragmentation function is used to estimate the momentum carried by the b-hadron with respect to that of the b-quark after quark fragmentation. The fragmentation function included in PYTHIA originates from a detailed study of the b-quark fragmentation function in comparison with OPAL [8] and SLD [9] data. To assess the impact of the b-fragmentation, the nominal parameters of the PYTHIA fragmentation function are replaced by the values from a tune using the Professor framework [10]. In addition, the nominal fragmentation function is replaced by the modified Bowler-Lund fragmentation function [11]. The b-jet response uncertainty is evaluated from the ratio between the response of b-jets in the varied Monte Carlo samples to the nominal PYTHIA. The response variations are well within 2%.

The b-jet JES uncertainty is obtained adding the calorimeter response uncertainty and the uncertainties from the systematic Monte Carlo variations in quadrature. The resulting additional JES uncertainty for b-jets is shown in Fig. 1.2. It is about 2% up to $p_T \approx 100$ GeV and below 1% for higher p_T. To obtain the overall b-jet uncertainty this uncertainty is added in quadrature to the JES uncertainty for inclusive jets.
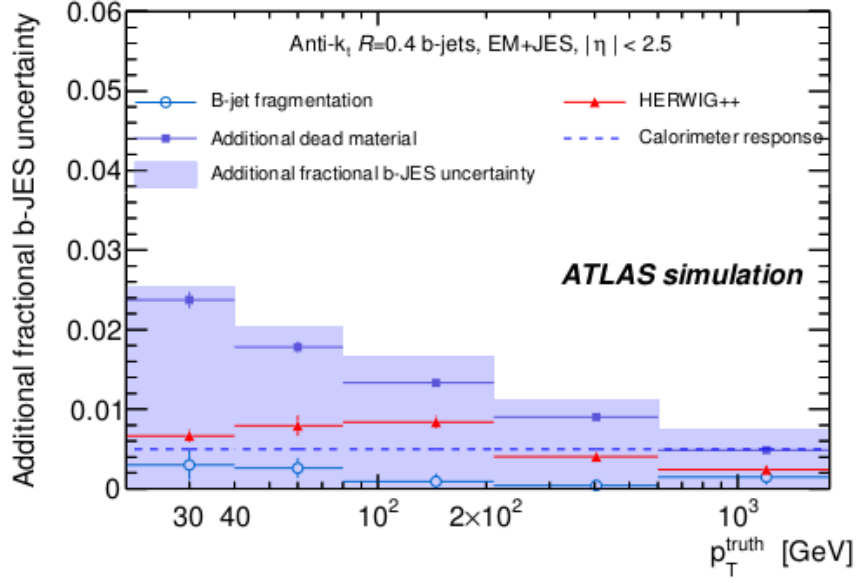
Figure 1.2: Additional fractional b-jet JES uncertainty as a function of the truth jet transverse momentum for anti-kt jets with $R = 0.4$ calibrated with EM+JES scheme for $|\eta| < 2.5$. Shown are systematic Monte Carlo variations using different modelling of the b-quark fragmentation and physics effects as well as variations in the detector geometry and the uncertainty in the calorimeter response to b-jets as evaluated from single hadron response measurements. Uncertainties in the individual points are statistical only.

12

1.2 Reconstruction of charged particle tracks

The Inner Detector layout and the characteristics of its main sub-detectors were presented in Section **??** of Chapter **??**. The tracking algorithm is based on a modular software framework, which is described in more detail in Ref. [12]. The main steps of the tracking algorithm are the following:

- Firstly, the raw data from the pixel and SCT detectors are converted into clusters, while the TRT raw timing information is turned into calibrated drift circles. The SCT clusters need to be further transformed into space-points, by combining the clusters information from opposite sides of the SCT module (stereo strip layers).

- In a second stage, the track-finding is performed, in which the pattern recognition and a global χ^2 minimization procedure is implemented as a default.

In the track-finding stage, track seeds are found in the first three pixel layers and in the first SCT layer. These are extended throughout the SCT to form track candidates and a first track fit is performed. Afterwards, ambiguities in the track candidates found in the silicon detectors are resolved, and tracks are extended into the TRT (which covers up to $|\eta| < 2.$). The final track candidate is refitted with the full information from the three tracking subdetectors. The baseline algorithm is designed for the efficient reconstruction of primary charged particles. Primary particles are defined as particles with a meanlife of greater than 3×10^{-11} s directly produced in a proton-proton interaction, or from the subsequent decays or interactions of particles with lifetime shorter than 3×10^{-11} s. The tracks reconstructed in this stage are required to have $p_T > 400$ MeV.

In a complementary stage, a track search starts from segments recon-structed in the TRT and extends them inwards by adding silicon hits, which is referred to as "back-tracking". This recovers tracks for which the first hits in the pixel layers are missing, e.g. because they originate from secondaries, which are produced in the interaction of primaries.

The final reconstructed track trajectory is usually defined at its closest point to the interaction region on the transverse plane by its impact param-eters in the transverse plane and in the longitudinal direction, respectively called d_0 and z_0[2], and by its momentum, typically expressed in azimuthal angle ϕ, polar angle θ and inverse momentum $1/p$.

The track reconstruction efficiency is defined as the fraction of primary particles with $p_T > 400$ MeV and $|\eta| < 2.5$ matched to a reconstructed track. The reconstruction efficiency for primary tracks with transverse momentum above 1 GeV and central η is above 80%, reaching values below 70% for tracks at the edge of the Inner Detector acceptance. The dense environment of a jet decreases the track reconstruction efficiency and increases the fake rate. This is caused by the ocurrence of shared hits between different tracks, which makes the pattern recognition and track fitting tasks more difficult.

The relative transverse momentum scale and resolution of tracks is defined as the Gaussian mean and width of

$$p_T{}^{MC} \times (1/p_T{}^{MC} - 1/p_T{}^{reco}) = 1 - \frac{p_T{}^{MC}}{p_T{}^{reco}} \tag{1.5}$$

where $p_T{}^{MC,reco}$, refers to the track's transverse momentum given by sim-ulation truth (MC) or by reconstruction (reco). It should be noted that the $(1/p_T)$ resolution is used instead of $\sigma(p_T)$ as the Inner Detector measures the

---

[2]Stricktly speaking the impact parameter is $|z_0|sin\theta$, where θ is the polar angle of the track.

sagitta and not directly the transverse momentum[3]. However, the resolution obtained from the equation above is the relative transverse momentum resolution, $\sigma(p_T)/p_T$. At low p_T the multiple scattering dominates the resolution, and at high momenta, the resolution is limited by the bending power of the solenoid field and by the instrinsic detector resolution. For a central track with $p_T =5$ GeV the transverse momentum resolution is around 75 MeV and the transverse impact parameter resolution is about 35 μm.

1.3   Vertex reconstruction

Primary vertices are reconstructed using an iterative vertex finding algorithm [13]. In a first step, a dedicated vertex finding algorithm associates tracks to vertex candidates. Vertex seeds are obtained by looking for the global maximum in the distribution of the z coordinates of the tracks. In a second stage, an iterative χ^2 fit is made using the seed and nearby tracks. Each track carries a weight which is a measure of its compatibility with the fitted vertex depending on the χ^2 of the fit. Tracks displaced by more than 7σ from the vertex are used to seed a new vertex and the procedure is repeated until no additional verteces can be found. The parameters of the beam spot are used both during the finding to preselect compatible tracks and during the fitting step to constrain the vertex fit.

The knowledge of the position of the primary interaction point (primary vertex) of the proton-proton collision is important for b-quark jets identification since it defines the reference point with respect to which impact parameters and vertex displacements are measured. The typical vertexing resolution in z is $O(100\mu\text{m})$.

---

[3]The relation between sagitta s and transverse momentum (p_T) is given by $s \sim 1/p_T$.

To ensure a good resolution on the vertex position, the primary vertex must be reconstructed from at least five tracks. The choice of the primary vertex is less trivial in the presence of minimum-bias events from pile-up: the primary vertex from a pile-up event may be mistakenly used as the signal vertex, or a fake primary vertex built from tracks from two different vertices may be reconstructed. The current strategy is to choose the primary vertex candidate that maximizes $\sum_{tracks} p_T{}^2$.

1.4 b-jet Tagging

The ability to identify jets originating from *bottom*-quarks (denoted as b-tagging in the following) is important for the high-p_T physics program of a general-purpose experiment at the LHC such as ATLAS since many interesting physics processes contain b-quarks in the final state, while the most abundant backgrounds contain mostly up, down and strange quark or gluon jets or, in a smaller fraction of cases, charm quark jets. The aim of b-tagging is therefore to identify the b-quark jets with high efficiency, while rejecting most of the background contamination from jets originating from the fragmentation of light (u, d, and s) quarks, gluons and c-quarks.

A b-quark, once produced, fragments necessarily into a b-flavoured hadron, b-hadron in the following. In most of the cases ($\approx 87\%$), first an excited b-hadron, like a B^* or a B^{**}, which decays inmediately, strongly or electro-magnetically, into a ground state b-hadron plus one or more further particles; while in the remaining cases, a ground state b-hadron is produced directly. One is only interested in the transition from a b-quark into the final state b-hadron, since the typical timescale for electromagnetic or strong interactions is so small that the B^*, B^{**} decay vertices are not significantly displaced

16

with respect to the primary vertex. In most of the cases ($\approx 91\%$) a B-meson is produced out of the fragmentation of an original b-quark (40% B^+, 40% B^0 and 11% B_s^0). The rest are b-baryons.

Due to the b-quark fragmentation function being very hard, most of the original b-quark energy is transmitted to the final b-hadron. This fraction is for example 70% for b-quarks with a momentum of $\approx$45 GeV. This property can be exploited during b-tagging, since the fragmentation for light quarks into light hadrons or c-quarks into c-hadrons is softer.

Any of the finally produced b-hadrons decay through weak interactions and therefore have a significant lifetime, which is on average, for all b-hadrons considered, $(1.568 \pm 0.009) \times 10^{-12}$ s. The effective distance travelled in the detector by the b-hadron before decaying depends on the b-hadron momentum, which enters the relativistic boost factor $\beta\gamma$. A b-quark with momentum of 50 GeV will travel around 3 mm, which is a visible flight length in the detector. Due to the combination of the b-hadron lifetime and relatively high mass ($m_B \approx 5.28$ GeV), which results in a non-negligible decay angle of the b-hadron decay products with respect to the b-hadron flight direction, the charged particles produced at the decay vertex will be on average significantly displaced with respect to the primary vertex position.

This is the main signature which is exploited by the $lifetime$ based b-tagging algorithms, which are based either on the presence of significantly displaced tracks, as in impact parameter based b-tagging algorithms, or on the explicit reconstruction of the b-hadron decay vertex, as in secondary vertex based b-tagging algorithms.

b-hadrons decay preferably into a c-hadron plus additional particles[4]. The lifetime of a c-hadron is not much lower than for b-hadrons, but in general

---

[4]Weak decays are governed by the CKM matrix mechanism, and $|V_{cb}|^2 >> |V_{ub}|^2$.

the momentum of the c-hadron will be lower than the original b-hadron momentum. However, the c-hadron can still travel for a significant path in the detector and form with its decay producs a visible *tertiary* vertex.

Another property which is usually exploited by b-tagging is the fraction of b- and c-hadron decays into leptons: a lepton from the semi-leptonic decay of a b-hadron ($b \rightarrow l$) or from the subsequent c-hadron decay ($b \rightarrow c \rightarrow l$) is produced in a b-quark in $\approx 21\%$ of the cases. This is valid both in case the lepton is a an electron or a muon, which brings the overall fraction of b-quarks ending up into a lepton to $\approx 42\%$. Due to the b- or c-hadron mass, the lepton will be emitted with an average transverse momentum comparable with m_{b-had} or m_{c-had}. By identifying either an electron or a muon originating from a jet and by requiring it to have sufficiently high p_T with respect to the jet axis, it is possible to identify b-jets.

Association of tracks to jets

The b-tagging performance relies criticaly on the accurate reconstruction of the charged tracks in the ATLAS Inner Detector. The actual tagging is performed on the sub-set of tracks in the event that are associated to jets. The b-tagging algorithm takes as input the three-momenta of the jets, reconstructed by a jet algorithm, and uses the jet direction to associate the charged particles tracks to the jet. Since the 2 Tesla solenoidal magnetic field of the ATLAS Inner Detector bends charged particles in the transverse plane, in particular in the case of low p_T tracks, the tracks are best matched to the jet by using the direction of their momenta at the point of closest approach to the interaction region. The criterion for associating charged particle tracks to jets is simply:

$$\Delta R(jet, track) < \Delta R_{cut} \qquad (1.6)$$

where usually the value of $\Delta R_{cut} = R$ is used; with R, the distance parameter of the jet algorithm used for jet reconstruction.

After the tracks are associated to the jets, they are filtered in order to remove tracks with bad quality or which can easily be erroneously identified as secondary tracks from b-decays. These include tracks originating from decays of even longer lived particles, like K_s^0 (c$\tau \approx$2.69 cm) and Λ baryons (c$\tau \approx$7.89 cm); from electromagnetic interactions in the detector material, like conversions in electron-positron pairs ($\gamma \to e^+ e^-$); or from hadronic interactions with the detector material, which result in two or more tracks with high impact parameter. In order to reject badly reconstructed tracks, quality cuts are applied. Requirements are imposed on the number of silicon hits, the track fit quality, the track momentum, and the transverse and longitudinal impact parameters. The track selection needs to be particularly tight in the case of the impact parameter based b-tagging algorithms, since in that case the explicit presence of a vertex is not required, so that the influence of badly reconstructed tracks or tracks from long lived particles does directly limit the performance. The minimum track p_T required is of 1 GeV in the case of the impact parameter based algorithms and of 400-500 MeV otherwise. The transverse and longitudinal impact parameters must fullfill $|d_0| <$1 mm (3.5 mm) and $|z_0| \sin \theta < 1.5$ mm (no cut on z_0) in the case of the algorithms relying on the impact parameters of tracks (on the reconstruction of secondary vertices). The minimum number of precision hits required is typically of 7 hits, for both approaches.

1.4.1 b-tagging algorithms

For the 2011 data-taking a set of lifetime taggers were commissioned and calibrated. In this section a brief description of the main features of these

algorithms will be given.

Impact parameter based b-tagging algorithms

The charged particle tracks originating from b-hadrons are expected to have significantly higher transverse and longitudinal impact parameters compared to prompt tracks originating directly from fragmentation. If the effect of long lived particles, conversions and hadronic interactions can be reduced, the best discrimination between prompt tracks and displaced tracks from b- and c-hadron decays can be obtained using the impact parameter significance, both in the transverse and longitudianl plane. Being,

$$IP_{r\phi} = d_0 \ \text{ and } \ IP_z = z_0 \sin\theta, \tag{1.7}$$

The transverse and longitudinal impact parameter significances are obtained by dividing $IP_{r\phi}$ and IP_z by their respective errors,

$$IP_{r\phi}/\sigma(IP_{r\phi}) \ \text{ and } \ IP_z/\sigma(IP_z). \tag{1.8}$$

On the basis that the decay point of the b-hadron must lie along its flight path, and in order to increase the discriminating power of the impact parameter significance, a lifetime sign is assigned to these variables (replacing the sign of the geometrical definition of the impact parameter). The sign is positive if the track extrapolation crosses the jet direction in front of the primary vertex (i.e. is more compatible with having its origin in a secondary decay vertex in the direction of flight expected for the b-hadron) or negative if the track is more likely to intersect the flight axis behind the primary vertex, opposite to the jet direction. Both cases are illustrated in Fig. 1.3.

The lifetime sign can be defined in three-dimensions, acording to the variables $\vec{p_{Tjet}}$, $\vec{p_{Ttrk}}$ and $\vec{\Delta r}_{IP} = \vec{r}_{IP} = \vec{r}_{PV}$, the three-dimensional impact
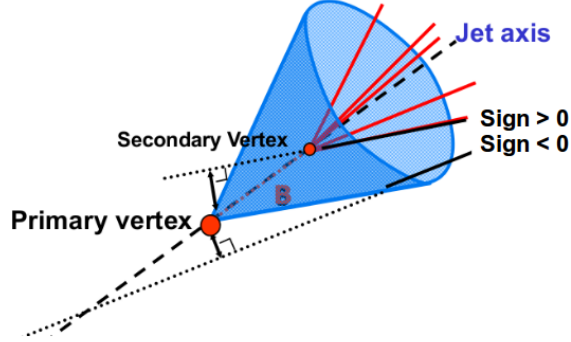
20

Figure 1.3: Lifetime sign of tracks. A positive and a negative lifetime signed track is shown.

parameter of the track with respect to the primary vertex:

$$sign_{3D} = sign([\vec{p}_{trk} \times \vec{p}_{jet}] \cdot [\vec{p}_{trk} \times \vec{\Delta r}_{IP}]). \quad (1.9)$$

The computation of the lifetime sign assumes that the jet direction reproduces, up to a good approximation, the b-hadron direction. Under this assumption and up to resolution effects both on the jet direction and on the impact parameter and momentum of the track, the lifetime sign of tracks originating from b-hadron decays is positive.

The lifetime sign can also be defined on the transverse plane $(x - y)$ or on the longitudinal plane $(r\phi - z)$ by considering respectively the transverse and longitudinal impact parameters (the projections of the three-dimensional impact parameter on the respective planes):

$$\text{sign}_{r\phi} = \text{sign}(\sin(\phi_{jet} - \phi_{trk}) \cdot d_{0,trk}); \text{ and } \text{sign}_z = \text{sign}((\eta_{jet} - \eta_{trk}) \cdot z_{0,trk}).$$
$$(1.10)$$

Tracks from the fragmentation in light-jets tend to have a signed impact parameter distribution which is symmetric around 0, since they have no

correlation with the jet direction. Tracks from b- and c-hadron decays, as expected, have an asymmetric distribution, with the most significant contribution at positive significances; however a negative tail extending beyond the pure fragmentation contribution is also seen, corresponding to resolution effects and to an eventual mismatch between the b-jet and the b-hadron directions.

The significance, which gives more weight to tracks measured precisely, is the main ingredient of the tagging algorithms based on impact parameters. Now, the impact parameter significance of all N tracks associated to the jet to tag need to be combined into a single discriminating variable. It is assumed that tracks are uncorrelated, so their probability density functions (PDF), defined based on the transverse and/or longitudinal impact parameter significance distributions for the different hipothesis, are uniquely defined as a function of the jet flavour. Using a likelihood function defined according to the product of these PDFs, under the hypothesis of uncorrelated tracks, the following likelihood ratio provides the optimal separation, according to Neyman-Person lemma [14]:

$$\mathrm{LR}(IP_1, IP_2, ..., IP_N) = \frac{\prod_{i=1}^{N} \mathrm{PDF}_b(IP_i)}{\prod_{i=1}^{N} \mathrm{PDF}_l(IP_i)} \tag{1.11}$$

For convention, the discriminant variable used for b-tagging is then defined as:

$$\mathrm{weight}(IP_1, IP_2, ..., IP_N) = \log(\mathrm{LR}(IP_1, IP_2, ..., IP_N)) \tag{1.12}$$

Using such a formalism, two impact parameter based b-tagging algorithms are constructed, based on the definition of $\mathrm{PDF}(IP_i)$:

- 1. IP2D: $\mathrm{PDF}(IP_i) = \mathrm{PDF}(IP_{i,r\phi})$

- 2. IP3D: $\mathrm{PDF}(IP_i) = \mathrm{PDF}(IP_{i,r\phi}, IP_{i,z})$

In the first case the track PDF is one-dimensional, based on the transverse impact parameter significance. In the second case the PDF is based on a two-dimensional histogram of the transverse and longitudinal impact parameter significance.

The **IP3D** is one of the high-performance tagging algorithms supported for the 2011 data-taking, in which input variables are compared to pre-defined smooth Monte Carlo PDFs for both b-jet and light jet hypotheses [15]. Prior to the use of these advanced tagger, a simpler tagging algorithm, the **Jet-Prob**, combining the impact parameter significances of all tracks associated to the jet was devised to be used for early data, being extensively used during 2010 [16].

The impact parameter based algorithm permits to obtain a very good b-tagging performance, as will be shown at the end of this chapter. This performance can be improved by using some information from the secondary vertex based vertexing algorithms in two aspects: tracks associated to long lived particle vertices can be removed from the tracks considered for the impact parameter based algorithms; and, the direction between the secondary and the primary vertex positions can be used to improve the reliability of the lifetime sign, substituting $\vec{p}_{jet}$ with $\vec{r}_{SV} - \vec{r}_{PV}$. The latter improves significantly the estimation of the b-hadron direction. Both kinds of information improve the performance of the impact parameter based b-tagging algorithms.

Secondary vertex based b-tagging algorithms

The typical topology of particle decays in a b-jet is a decay chain with two vertices, one steaming from the b-hadron decay and at least one from c-hadron decays. The reconstruction of these secondary vertices is done in an inclusive way, where the number of charged particle tracks originating from the b- and

23

c-hadron decays is not known a-priori. An exclusive reconstruction of the huge number of different possible *b*-decay modes cannot be performed, the set of selection cuts needed to reconstruct all of them would severely limit the reconstruction efficiency.

Two strategies to detect a secondary decay vertex in *b*-jets are available in ATLAS. The first one is based on the fit of a single geometrical vertex. Even if this hypothesis is not correct, this approximation works well for a large fraction of cases. The second algorithm is based on a kinematic approach, which assumes that the primary event vertex and the *b*- and the *c*-hadron decay vertices lie approximately on the same line, the flight path of the *b*-hadron.

The inclusive fit of a single displaced vertex in *b*-jets is based on the VKalVrt [17] reconstruction package. The main idea of the algorithm implemented in this package is to maximise the *b/c*-hadron vertex detection efficiency, keeping at the same time the probability to find a vertex inside a light jet low.

The algorithm starts with all tracks associated to the jet and passing a loose cut selection. The vertex search starts with looking for all track pairs and trying to form a two-track vertex. Each track of the pair must have a three-dimensional impact parameter significance with respect to the primary vertex larger than 2σ and the sum of these two significances must be larger than 6σ. To reduce the influence of badly measured tracks, the two-tracks vertices are required to be produced in the direction of flight of the *b*-quark, by requiring the scalar product of $(\vec{r}_{2-track} - \vec{r}_{PV}) \cdot \vec{p}_{jet}$ to be positive. Charged particles coming from long lived particles and conversions are not considered for the inclusive *b*-decay vertex fit. All the tracks corresponding to the accepted two-track vertices are used to determined a single secondary

vertex. If the resulting vertex has a very small vertex probability, the track with the highest constribution to the vertex χ^2 is removed from the vertex fit and the vertex fit is repeated until the χ^2 of the vertex fit is good. The result of this procedure is the (eventual) presence of a vertex, its position, and the list of its associated tracks.

The **SV1** secondary vertex algorithm uses this procedure to reconstruct inclusive secondary vertices. This advanced tagger takes advantage of three of the reconstructed vertex properties: the invariant mass of all tracks associated to the vertex, the ratio of the sum of the energies of the tracks in the vertex to the sum of the energies of all tracks in the jet, and the number of two-track vertices. These variables are combined using a likelihood ratio technique. SV1 relies on a two-dimensional distribution of the two first variables and a one-dimensional distribution of the number of two-track vertices. In addition the distance ΔR between the jet axis and the line joining the primary vertex to the secondary one is used.

The three-dimensional decay length significance alone, signed with respect to the jet direction can be used as a discriminating variable between b-jets and light jets: this is the principle of the early data **SV0** tagger, extensively used as well with the 2010 and 2011 data [18].

As opposed to the algorithm described above, in which the displaced tracks are selected and an inclusive single vertex is obtained, a second algorithm, called **JetFitter**, is based on a different hypothesis. It assumes that the b- and the c-hadron decay vertices lie on the same line defined through the b-hadron flight path. All charged particle tracks stemming from either decay intersect this b-hadron flight axis. This method has the advantage of reconstructing imcomplete topologies, with, for instance, a single track from the b-hadron and a single track from the c-hadron decay. The fit in this

25

case evaluates the compatibility of the given set of tracks with a b-c-hadron like cascade topology, increasing the discrimination power against light quark jets. The lateral displacement of the c-hadron decay vertex with respect to the b-hadron flight path is small enough not to violate significantly the basic assumption within the typical resolutions of the tracking detector. The discrimination between b-, c- and light jets is based on a likelihood using similar variables as in the SV1 tagging algorithm above, and additional variables such as the flight length significances of the vertices.

Algorithm combinations and performance

The IP3D and SV1 tagging algorithms both use the likelihood ratio method, and due to this they can be easily combined: the weights of the individual tagging algorithms are simply summed up.

The combination of the JetFitter and the IP3D algorithms can be performed using an artificial neural network technique with Monte Carlo simulated training samples and additional variables describing the topology of the decay chain.

Figure 1.4 compares the performance for the various ATLAS b-tagging algorithms described in a simulated sample of $t\bar{t}$ events. It can be seen that by combining the vertexing techniques and the impact parameter information, the IP3D+SV1 and IP3D+JetFitter algorithms can reach very high tagging efficiencies.

The performance of a b-tagging algorithm is usally measured in terms of the *light-jet rejection* obtained for a given *b-jet tagging efficiency*. Curves are obtained by varying continuously the *operating point* of each tagger, i.e. the cut on its output discriminating variable (weight). The b-jet tagging efficiency, ϵ_b, is the fraction of jets labeled as b-jets that are properly tagged

while the light-jet rejection, defined as $1/\epsilon_{light}$, is the reciprocal of the fraction of jets that are labeled as light jets and are actually tagged incorrectly by the algorithm. The labeling procedure used for b-tagging is based on the flavor of true quarks: a jet is labeled as a b-quark jet if a b-quark is found in a cone of size $\Delta R = 0.3$ around the jet direction. The various labeling hypotheses are tried in this order: b quark, c quark and τ lepton. When none of these hypotheses are satisfied, the jet is labeled as a light jet. No attempt is made to distinguish light jets originating from gluons from those originating from quarks at this stage.
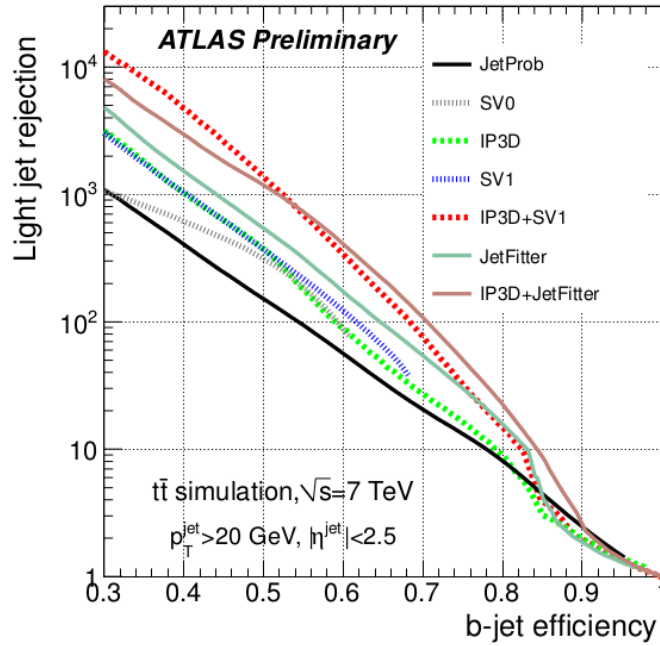
Figure 1.4: Light-jet rejection as a function of the b-jet tagging efficiency for the early tagging algorithms (JetProb and SV0) and for the high-performance algorithms, based on simulated $t\bar{t}$ events.

The MV1 tagging algorithm

The **MV1** b-tagging algorithm is a combined algorithm based on a neural network using the output weights of the JetFitter+IP3D combination, IP3D and SV1 algorithms as input. For being the best performing algorithm (better light rejection for the same signal efficiency) it is the recomended tagger for 2011 and 2012 analyses. This is the b-tagging algorithm used in this thesis.

1.4.2 b-tagging calibration

In order for b-tagging to be used in physics analyses, the efficiency with which a jet originating from a b-quark is tagged by a b-tagging algorithm needs to be measured in data. Morover, an appropriate description of the b-tagging efficiencies based on measurements with data is essential for correctly modelling the measurements in Monte Carlo simulation . A second necessary piece of information is the probability of mistakenly tagging a jet originating from a light-flavour (u-, d-, s-quark or gluon) jet as a b-jet, referred to as the mistag rate. The b-tagging "calibration" includes both the measurement of the mis-tag rates and b-tagging efficiency.

The measurements of the b-tag efficiency and mistag rate are provided in the form of jet p_T- and η-dependent scale factors that correct the b-tagging performance in simulation to that observed in data. The scale factors are defined as the ratio of the b-tag efficiency or mistag rate in data and simulation:

$$\kappa_{\epsilon_b}^{data/sim} = \frac{\epsilon_b^{data}}{\epsilon_b^{sim}}, \;\; \kappa_{\epsilon_l}^{data/sim} = \frac{\epsilon_l^{data}}{\epsilon_l^{sim}}, \tag{1.13}$$

where ϵ_b^{sim} and ϵ_l^{sim} are the fractions of b- and light-flavour jets which are tagged in simulated events, with the jet flavour defined by matching to gen-

erator level partons as defined in the previous section.

In physics analyses, these p_T-dependent scale factors are then applied as weights to the jets in Monte Carlo simulation, to reproduce the b-tagging performance in data.

The main b-tagging efficiency calibration methods, the so called *system8* and p_{rel} methods are described in detail in ref [19].These measurements are based on a sample of jets with muons inside, where the muons are serving as a reference b-tagging algorithm to obtain a b-jet sample on which the calibrations can be performed. At the LHC, the large $t\bar{t}$ production cross section of $\sigma_{t\bar{t}} = 1773(\text{stat.})+8(\text{sys.})7(\text{lum.})$ pb [20] offers an alternative source of events enriched in b-jets. Calibrations using samples of $t\bar{t}$ events have been obtained for SV0, IP3D+SV1, JetFitter and MV1 b-tagging algorithms [21]. All these algorithms provide an output weight w, discriminating between b-jets and non-b-jets. Lower values of w are assigned to c- and light-flavour jets, whereas the purity of b-jets increases with w. For each b-tagging algorithm a set of operating points, corresponding to a certain w cut value, are defined and calibrated:

- SV0: $\epsilon_b^{sim} = 50\%$

- IP3D+SV1: $\epsilon_b^{sim} = 60\%$, $\epsilon_b^{sim} = 70\%$, $\epsilon_b^{sim} = 80\%$

- JetFitter: $\epsilon_b^{sim} = 57\%$, $\epsilon_b^{sim} = 60\%$, $\epsilon_b^{sim} = 70\%$, $\epsilon_b^{sim} = 80\%$

- MV1: $\epsilon_b^{sim} = 60\%$, $\epsilon_b^{sim} = 70\%$, $\epsilon_b^{sim} = 75\%$, $\epsilon_b^{sim} = 85\%$

where ϵ_b^{sim} is the nominal b-tagging efficiency derived from an inclusive sample of simulated $t\bar{t}$ events.

The mistag rate is measured in data using two methods, both based on an inclusive sample of jets, referred to as the *negativetag* and *sv0mass*

methods [**?**]. The first method uses the invariant mass spectrum of tracks associated with reconstructed secondary vertices to separate light and heavy-flavour jets, and the other is based on the rate at which secondary vertices with negative decay length, or tracks with negative impact parameter, are present in the data.

Currently, there is no explicit measurement of the c-tag efficiency available in ATLAS. As both the b- and c-tag efficiencies are dominated by decays of long-lived heavy flavour hadrons, they are expected to show a similar behaviour. In general, for physics analyses, it is thus assumed that the scale factor is the same for b- and c-jets. However, to take into account possible deviations from this assumption, the systematic uncertainty for the c-tag efficiency scale factor is inflated by a factor of two, which is considered to be a conservative choice based on simulation studies. In the future, the c-tag efficiency will be measured in dedicated analyses.

Chapter 2

Double b-hadron jet identification

In this chapter we focus on the understanding of the internal structure of b-jets containing two b-hadrons by investigating the differences between these and single b-quark jets. These differences are expected to arise from the two-subjet structure of double b-hadron or "merged" jets, which would tend to be wider and with a larger number of constituents. Based on these envisaged characteristics, simulated QCD samples of b-tagged jets were used to explore properties with potential discrimination power. The Monte Carlo distributions were compared to data from the 2011 run for validation. We present results from these studies and discuss the choice of the observables selected to build the multivariable tool presented in Chapter ??.

2.1 Data Analysis

The tagging technique presented in this thesis relies on Monte Carlo predictions for the signal (single b) or background (merged b) hypotheses. The accuracy of the simulation is validated with data by comparing the distributions of the different variables studied.

The data samples employed correspond to proton-proton collisions at $\sqrt{s} = 7$ TeV delivered by the LHC and recorded by ATLAS between May and November 2011, with the LHC running with 50 ns bunch spacing, and bunches organized in bunch trains. Only data collected during stable beam periods in which all sub-detectors were fully operational are used. After the application of the data quality selection, the surviving data corresponds to an integrated luminosity of 4.7 fb^{-1}. The LHC instantaneous luminosity steadily increased during 2011. As a result, the average number of minimum-bias pile-up events, originating from collisions of additional protons in the same bunch as the signal collision, grew from from 3 to 20. This fact will be of importance when discussing the selection of discriminating variables.

The Monte Carlo event generators discused in Section **??** are used here. Samples of dijet events from proton-proton collision processes were simulated with PYTHIA version 6.423 [22], used both for the simulation of the hard $2 \rightarrow 2$ process as well as for the parton shower, underlying event, and hadronization models. The ATLAS AMBT2 tune of the soft model parameters was used [23]. In order to have sufficient statistics over the entire p_T spectrum, eight samples were generated with different thresholds of the hard-scattering partonic transverse momentum $\hat{p}_T$. Events from different samples were mixed taking into account their respective production cross sections. The simulated data sample used for the analysis gives an accurate description of the pile-up content and detector conditions for the full 2011 data-taking period.

2.1.1 Event selection

The event selection and quality criterion used to extract, from the data and Monte Carlo samples, the final set of jets for the analysis comprises different

steps:

- **Trigger**. The event sample was collected using the ATLAS single jet triggers which select events with at least one jet with transverse energy above a given threshold. At the hardware Level 1 and local software Level 2 (see Section **??**), cluster-based jet triggers are used to select events with high-pt jets. The Event Filter, in turn, runs the offline anti-k_t jet finding algorithm with $R = 0.4$ on topological clusters over the complete calorimeter. At this stage, the transverse energy thresholds, expressed in GeV, are: 20, 30, 40, 55, 75, 100, 135, 180. These triggers reach an efficiency of 99% for events having the leading jet with an offline energy higher than the corresponding trigger thresholds by a factor ranging between 1.5 and 2. The jet triggers with the lowest p_T thresholds were prescaled by up to five orders of magnitude.

- **Primary vertex**. The offline event selection requires at least one primary vertex candidate with 5 or more tracks. No requirements are placed on the longitudinal position (along the beam line) of the vertex as the beam spot is used as a constraint when fitting the vertex.

- **Primary jet algorithm**. The jet algorithm selected for the analysis was the ATLAS default anti-k_t algorithm [24], with a distance parameter $R = 0.4$, using calorimeter topological clusters [3] as input.

- **Jet calibration**. The EM+JES calibration scheme, described in Section1.1, was used to correct the jet energies for inhomogeneities and for the non-compensating nature of the calorimeter.

- **Jet quality**. Several quality criteria are applied to eliminate "fake" jets that are caused by noise bursts in the calorimeters and energy

depositions belonging to a previous bunch crossing [25].

- **Jet tagging**. Only jets tagged as b-jets using the MV1 b-tagging algorithm at the 60% efficiency working point were considered.

- **Isolation**. b-tagged jets with close-by jets ($\Delta R < 0.8$) with p_T higher than 7 GeV at electromagnetic scale were not included in the analysis.

All jets, with transverse momentum between 40 and 480 GeV, the selected p_T range for the analysis, were required to be in a region with full tracking coverage, $|\eta_{jet}| < 2.1$, and they were classified in eight p_T bins chosen such as to match the jet trigger 99% efficiency thresholds (in GeV): 40, 60, 80, 110, 150, 200, 270, 360. An event is used if it satisfies the highest threshold trigger that is 99% efficient for the p_T bin that corresponds to the p_T of its leading jet.

In the case of MC, the reconstructed b-tagged jets were further classified into single and merged b-jets based on truth Monte Carlo information. A b-hadron is considered to be associated to a jet if the ΔR distance in $\eta - \phi$ space between the direction of the hadron and the jet axis is smaller than 0.4. Jets were labeled as merged (single) b-jets if they contain two (only one) b-hadron:

$$\text{single } b\text{-jets: } \Delta R(j, b_{1/2}) < 0.4 \tag{2.1}$$

$$\text{merged } b\text{-jets: } \Delta R(j, b_1) < 0.4 \ \& \ \Delta R(j, b_2) < 0.4 \tag{2.2}$$

where j is a jet in the event and $b_{1/2}$ are the b-hadrons in the event. In the case another size parameter is used for jet finding, the definitions in equations 2.1 and 2.2 change accordingly.

2.1.2 Track selection

It is important to select genuine tracks belonging to jets. Only tracks located within a cone of radius $\Delta R(j, \text{track}) \leq 0.4$ around the jet axis were considered. Cuts on $p_T^{\text{trk}} > 1.0$ GeV and the χ^2 of the track fit, $\chi^2/ndf < 3$, are applied. In addition, tracks are required to have a total of at least seven precision hits (pixel or micro-strip) in order to guarantee at least 3 z-measurements. Tracks are also required to fulfill cuts on the transverse and longitudinal impact parameters at the perigee to ensure that they arise from the primary vertex. As cutting on impact parameter (IP) significance might be detrimental for b-jets, where large IP values are expected, relaxed cuts were used, $|d_0| < 2$ mm, and $|z_o \sin \theta| < 2$ mm, with θ being the polar angle measured with respect to the beam axis. The track quality cuts are summarized in table 2.1.

Track parameter	Selection
p_T	> 1 GeV
d_0^{PV}	< 2 mm
$z_0^{PV} \sin \theta$	< 2 mm
$\chi^2/ndof$	< 3
Number of Pixel hits	≥ 2
Number of SCT hits	≥ 4
Number of Pixel+SCT hits	≥ 7

Table 2.1: Track selection criteria used for double b-hadron jet tagging, where d_0^{PV} and z_0^{PV} denote the transverse and longitudinal impact parameters derived with respect to the primary vertex. The $chi^2/ndof$ is that of the track fit.

2.2 Kinematic differences between single and double b-hadron jets

The differences between genuine b-quark jets and double b-hadron jets, that in QCD originate mainly from gluon splitting, are expected to arise from the two-subjet structure of merged jets. In this section we present the study of a set of jet shape and substructure variables for the discrimination between single and merged b-jets. These variables are built from jet constituents either at calorimeter level (topological clusters) or tracks associated to the jet.

Jet track multiplicity The jet track multiplicity is a variable simple to calculate that carries important information of the jet inner structure. It is defined as the number of tracks with p_T above 1 GeV, satisfying the quality cuts described in section 2.1.2, and contained within a cone of radius $R = 0.4$ around the jet axis. Figure 2.1 shows its distribution for two p_T bins, representative of the range covered in this study. It is observed that merged b-jets contain on average around two more tracks than single b-jets at low jet p_T, with a larger difference at higher p_T values.

The effect of the minimum track p_T requirement was examined by lowering the selection cut to $p_T > 0.5$ GeV. On the one hand this could lead to an improvement in discrimination if it captured more information about the fragmentation process; on the other hand, a lower minimum track p_T can make the method more sensitive to pile-up with the addition of soft tracks incorrectly associated to the jets. It was observed that reducing the p_T cut of the tracks degrades the discrimination because it widens the distributions without increasing the separation between single and merged jets.

In order to evaluate the effect of using displaced tracks originating from
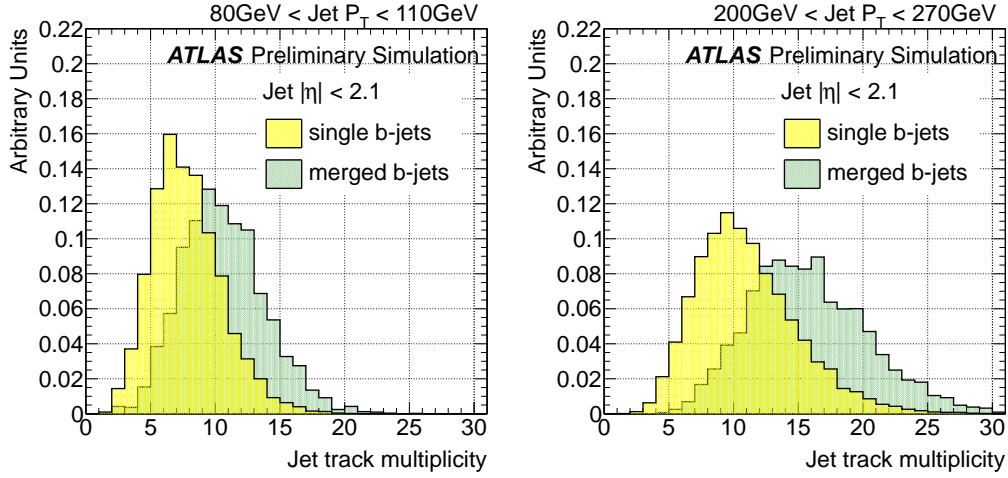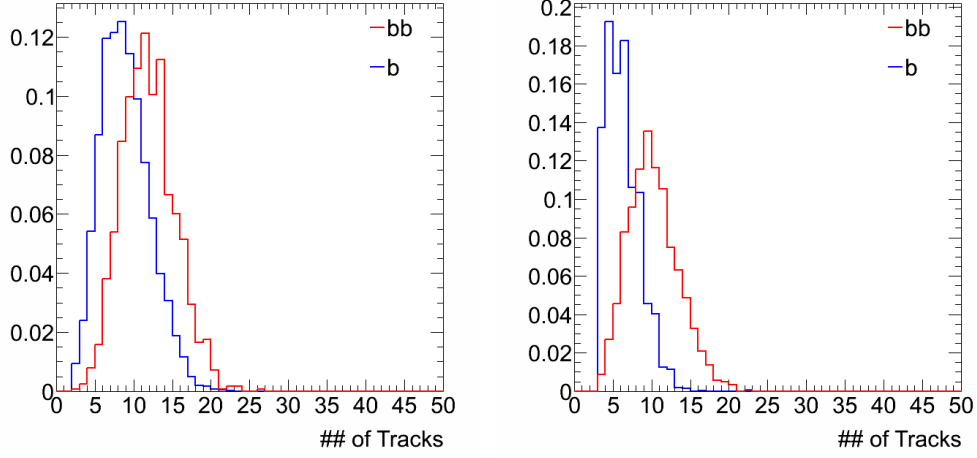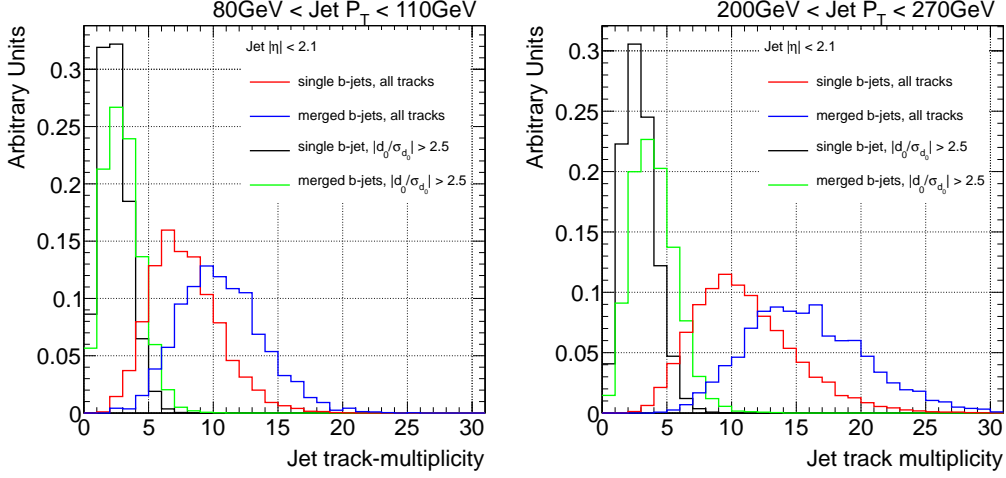
Figure 2.1: Distribution of the track multiplicity in jets for single and merged b-jets between 80 GeV to 110 GeV (left) and 200 GeV to 270 GeV (right).

the b-hadrons decays a preliminary study was done using a sample of dijet events generated with PYTHIA and with no detector simulation. For this study jets were reconstructed using all stable particles in the event, clustered with the anti-k_t algorithm. The association of charged particles was done in the same way as with the full ATLAS simluation. Distributions of the track multiplicity built using all charged particles and using only charged particles coming from the b-hadron decay ("b-tracks") are illustrated in in Fig. 2.2. A better discrimination between single and merged b-jets is observed when using b-tracks only. The result obtained with PYTHIA suggests that a potential improvement in single-merged separation can be achieved by circumscribing the track selection, in the full simluation, to tracks with large impact parameter significance. A comparison of track multiplicity distributions using all tracks and distributions built with displaced tracks is shown in Fig. 2.3. No improvement is obtained by using displaced tracks ($|d_0|/\sigma(d_0) > 2.5$). The potential sensitivity achieved by enriching the sample in tracks associated to

Figure 2.2: Distribution of the track multiplicity in jets for single (b) and merged (bb) jets between 80 GeV to 120 GeV in a sample of dijet events generated with PYTHIA and no detector simulation. Distributions are shown using all charged particles (left) and using only charged particles coming from b-hadron decay (right).

the b-hadron is counterbalanced by the lower number of associated tracks.

Jet width The jet width is part of a set of continuous variables that attempt to distinguish individual particles/subjets within the jet by means of smooth funcion of $(\Delta\eta, \Delta\phi)$ away from the jet axis, in order to form combinations like geometric moments. This particular combination is a linear moment which sums the distances between the jet constituents and its axes, weighted by the constituent p_T, and normalized to the total p_T of the jet. Its definition is,

$$Jet\ width = \frac{\sum_{i=1}^{N} p_T^{const_i} \Delta R(const_i, jet)}{\sum_{i=1}^{N} p_T^{const_i}} \tag{2.3}$$

where N is the total number of calorimeter, track or particle constituents.

This observable has been extensively used to discriminate between gluon initiated and light quark initiated jets, see for instance [26] and [27]. Gluon

38

Figure 2.3: Distribution of the jet track multiplicity single and merged b-jets between 80 GeV to 110 GeV (left) and 200 GeV to 270 GeV (right), for all and displaced tracks only.

jets are seen to be broader than quark jets. In the case of jets originating from b-quarks, these resemble gluon jets more closely than quarks jets [28]: due to the longer decay chain of b-hadrons the angular spread is larger for a b-jet than a light-quark jet. In order to explore how merged jets, originating from a gluon splitting into a $b\bar{b}$ pair, compare to single b-quark jets and pure gluon jets, a standalone PYTHIA analysis was performed. Figure 2.4 illustrates the result; b-jets containing two b-hadrons present a greater angular width relative to single b-jets and gluon initiated jets. The latter, in turn, looks broader than single for medium p_T jets. This behavior is somehow expected in the LHC's higher p_T jets because the QCD shower produces more particles resulting in broader gluon jets, whereas the particle multiplicity is relatively fixed in the b-hadron decay.

Distributions for the track-jet width with full ATLAS simulation are shown in Fig. 2.5. In this case the sum in equation 2.3 runs over the N

tracks associated to the jet, using the same criteria as for the jet track multiplicity. As expected, merged b-jets are wider than single b-jets.

PYTHIA standalone samples were also to used evaluate the potential gain in discrimination obtained by utilising all stable particles in the event to build the observable, as opposed to using the charged particles only. A 10% improvement in merged b-jet rejection (for a 50% efficiency in selecting single b-jets) was achieved.

In full simulation, the jet width can be measured in terms of calorimeter variables by replacing tracks by topological clusters in the sum. Although it offers good separation, this variable is more sensitive to the amount of pile-up in the event than its track-based counterpart. This is illustrated in Fig. 2.6, which shows the distribution of calorimeter width and track-jet width for single b-jets in events with low and high number of primary vertices (NPV) in a low p_T region where the effect of pile-up is more important.

In general, all the studied calorimeter-based jet variables show similar dependences with NPV. For this reason the track-based versions are preferred as more robust discriminators.

Jet Mass The jet mass, like the linear radial moment, depends on the radiation pattern of the event. It is the most basic observable for distinguishing massive boosted objects from jets originating from quarks or gluons. The latter are expected to be dominated by wide-angle emissions, with increased probability to see high mass jets initiated from gluons as opposed to quarks [29]. Detector level jet mass distributions for jets selected to have $80 < p_T < 110$ GeV and $200 < p_T < 270$ GeV are shown in Fig. 2.7, both for single and merged b-jets. Merged jets tend to have higher masses than single b-jets for the same p_T bin.

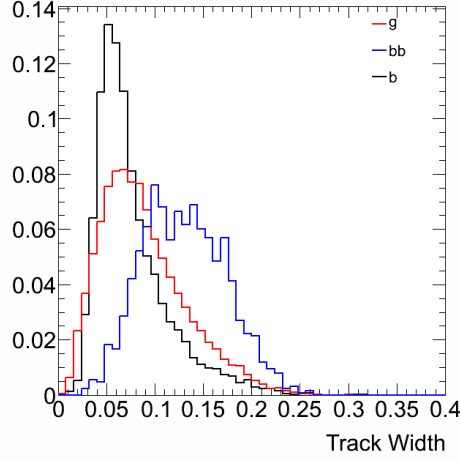Although it shows good separation, this calorimeter based variable can

40

Figure 2.4: Distribution of track-jet width in jets for gluon-initiated (g), single (b) and merged (bb) jets between 80 GeV to 120 GeV in a sample of dijet events generated with PYTHIA and no detector simulation.
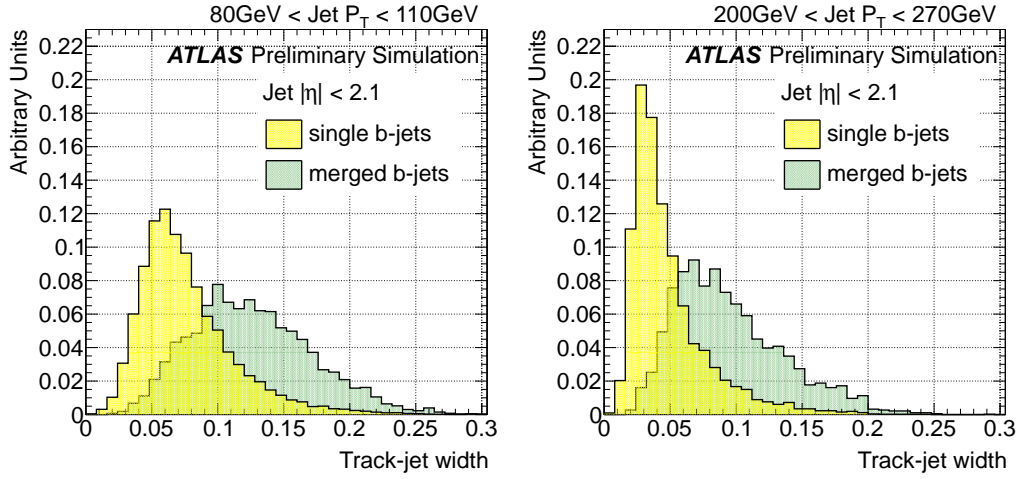

Figure 2.5: Distribution of track-jet width in jets for single and merged b-jets between 80 GeV to 110 GeV (left) and 200 GeV to 270 GeV (right).
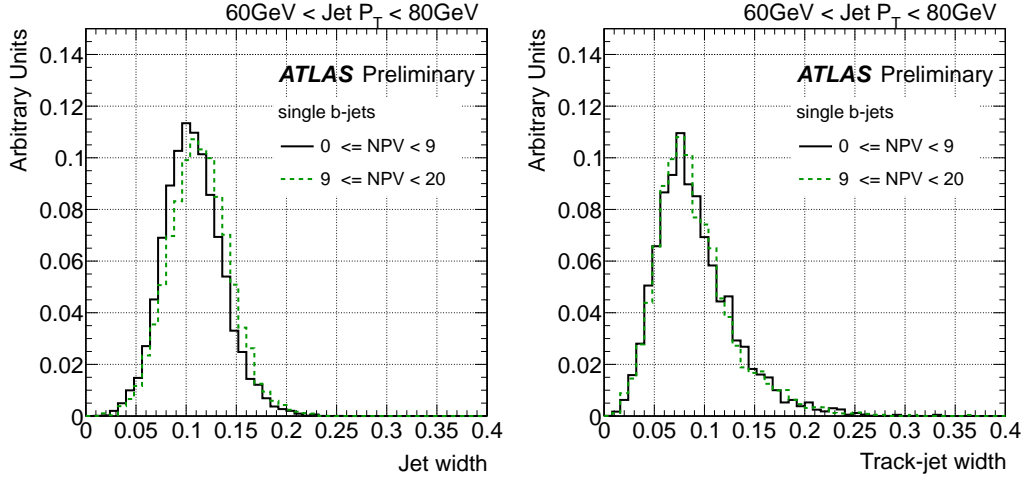
Figure 2.6: Distribution of jet width using topological clusters (left) and tracks (right) for single *b*-jets in two bins of number of primary vertices (NPV) for jets between 60 GeV to 80 GeV.

be significantly affected by the amount of pile-up in the event as even a single soft wide angle deposition will have an effect on the jet mass, shifting the distribution to higher values.

ΔR *between leading tracks* An alternative approach to measuring the width is to use the angular separation of the two hardest constituents inside jets. This has the advantage of removing any dependence on the shower development within the calorimeter and focuses on the hard components of the jet.

Figure 2.8 shows the distribution of the ΔR between leading tracks in the jet for single and merged *b*-jets. The merged *b*-jet distributions are slightly broader than single *b*-jet distributions for medium jet p_T. The effect diminishes as we go to higher transverse momentum values, offering very poor discrimination.

Maximum ΔR between track pairs Several other variables, besides the jet
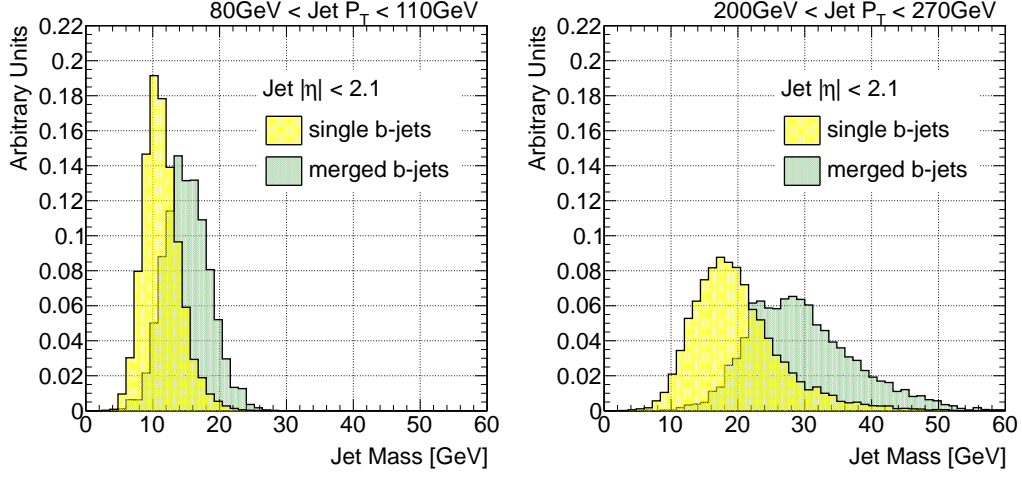
Figure 2.7: Distribution of jet mass in GeV for single and merged b-jets between 80 GeV to 110 GeV (left) and 200 GeV to 270 GeV (right).
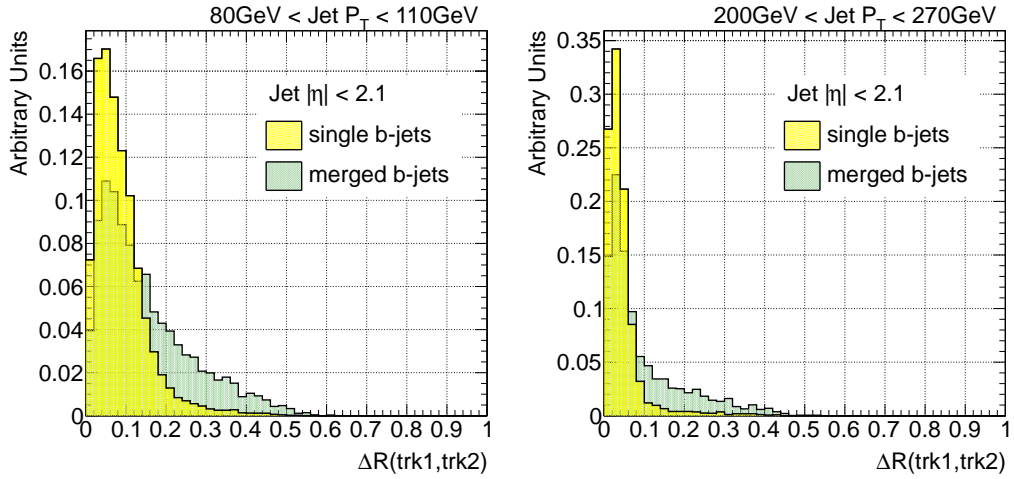

Figure 2.8: Distribution of ΔR between leading tracks for single and merged b-jets between 80 GeV to 110 GeV (left) and 200 GeV to 270 GeV (right).
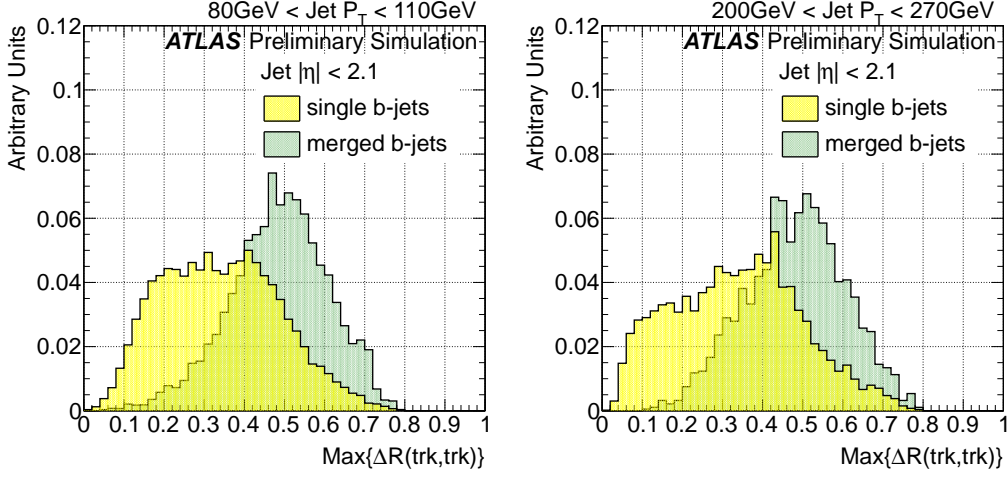
Figure 2.9: Distribution of the maximum ΔR between pairs of tracks in jets for single and merged b-jets between 80 GeV to 110 GeV (left) and 200 GeV to 270 GeV (right).

width, were investigated to expose the expected two-subjet substructure of merged b-jets. The maximum ΔR separation between pairs of tracks associated to the jet ($\max\{\Delta R(trk, trk)\}$) was also evaluated as a discrimating variable. Its distribution is shown in Fig. 2.9, for single and double b-hadron jets. The latter shows significantly higher values for this variable over a broad range of jet p_T. The distinct characteristic of this variable is that the separation between single b-jets and merged does not depend on jet p_T. In spite of its good discrimination power, alternative characterising variables are desirable as $\max\{\Delta R(trk, trk)\}$ is sensitive to soft tracks originating from pile-up.

Subjet multiplicity The subjet multiplicity − the number of subjets within a jet − provides information on the distribution of energy and multiplicity of particles within a jet. For instance, a measurement of this observable for quark and gluon jets indicates that gluon-initiated jtes tend to have on

44

average higher subjet multiplicity [30]. This result is consistent with the QCD prediction that gluons radiate more than quarks. In this case the k_t algorithm is rerun for subjet finding.

In general, by using the inclusive k_t or other sequential recombination algorithms, introduced in Section **??**, it is straightforward to define a "subjet algorithm" in which the structure of the jet constituents is resolved using either the same jet finder algorithm as used for jet reconstruction or a new one with a fixed (smaller) distance parameter. As an alternative to fixed distance parameter subjets, it is also possible to undo the last step in the recombination sequence [31] in order to identify the decay products of an object. This approach is used in several jet grooming procedures[1], see for instance [33].

Figure 2.10 shows the distribution of the number of subjets for single and merged b-jets. The subjets in this case were built using the associated tracks as constituents, clustered by the inclusive k_t algorithm with distance parameter $R = 0.2$. Merged jets tend to have on average one more subjet than single b-jets. The discrimination power of this variable is therefore very poor.

ΔR *between the axes of two k_t subjets* The ΔR between k_t subjets is obtained by applying the exclusive k_t algorithm [34] to the tracks associated to the jet using a large k_t distance parameter to ensure that all tracks get combined. The clustering is stopped once it reaches exactly two jets. The ΔR between the axes of the two exclusive subjets is shown in Fig. 2.11. As expected, it is larger for merged than for single jets. We observe that this variable provides very good separation, with the advantage of infrared safety

---

[1]Jet grooming comprises dedicated techniques to remove uncorrelated radiation within a jet. A review of these procedures can be found in [32].
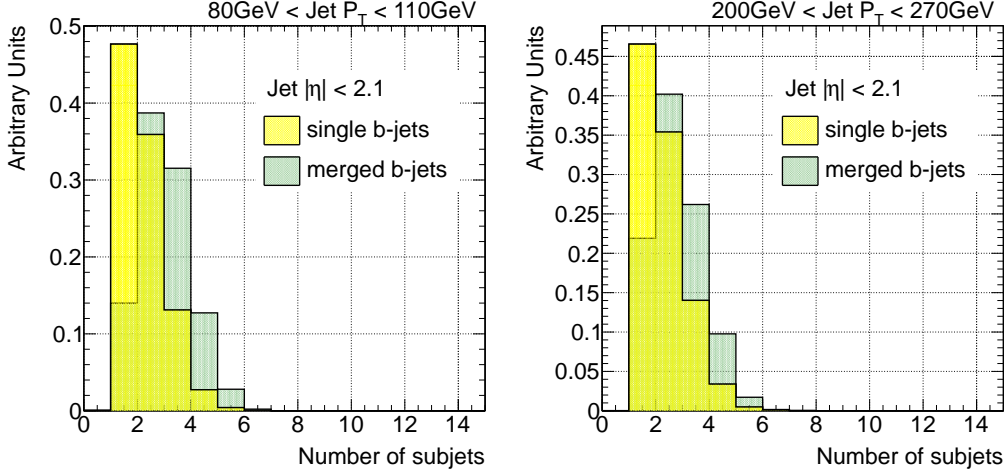
Figure 2.10: Distribution of the number of k_t sub-track-jets for single and merged b-jets between 80 GeV to 110 GeV (left) and 200 GeV to 270 GeV (right).

and insensitivity to pile-up as opposed to $\max\{\Delta R((trk, trk)\}$.

In order to illustrate how this variable works, an event display of a merged b-jet with a large (> 0.3) ΔR value is shown in Fig. 2.12. For this image, the jets active area [35] was reconstructed following a procedure called "ghost association", in which the event topoclusters plus a grid of 0.1×0.1 cells with nearly zero energy get associated to the jet through jet clustering. In the case of Figure 2.12 the anti-k_t algorithm was used. The event display indicates how the high energy cells in the jet with two b-hadorns are grouped around the b-hadrons directions, leading to the two-subjet substructure of merged jets.

N-subjettiness variables It is possible to extend the use of individual subjets in conjunction with more traditional jet shape variables. Using these tools, an inclusive jet shape based on the substructure topology of a single jet, "N-subjettiness" [36] is defined. This variable describes the energy
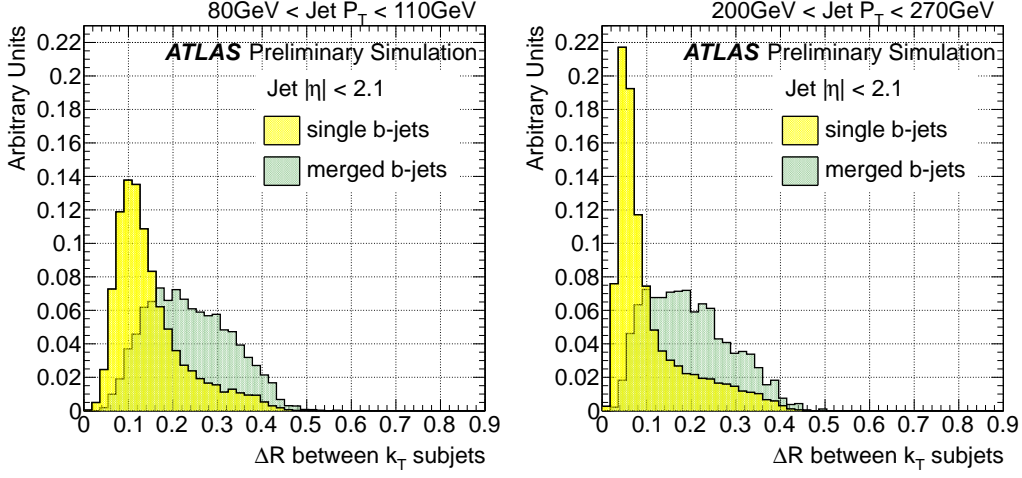
Figure 2.11: Distribution of the ΔR between the axes of the two k_t subjets in the jet for single and merged b-jets between 80 GeV to 110 GeV (left) and 200 GeV to 270 GeV (right).

flow within a jet, quantifying the degree to which radiation is aligned along specified subjet axes. This jet shape was adapted from the event shape N-jettiness [37].

Given candidate subjets directions determined by an external algorithm such as the exclusive k_t procedure, the variable is defined as,

$$\tau_N^{(\beta)} = \frac{1}{\sum_k p_{Tk} \, (R_0)^\beta} \sum_k p_{Tk} (\min\{\Delta R_{j1,k}, \, \Delta R_{j2,k}, ..., \Delta R_{jN,k}\})^\beta. \qquad (2.4)$$

The sum runs over the k constituents in a given jet where $p_{T,k}$ are their transverse momenta, and $\Delta R_{j1,k}$ is the distance between the candidate subjet $j1$ and a constituent particle k. R_0 is the characteristic jet radius used in the original jet clustering algorithm. The exponential weight, β, can optionally be applied to the angular distance computed between the subjets and the jet constituents. Since eq. 2.4 is linear in each of the constituent particle momenta, this variable is an infrared- and colliner-safe observable.

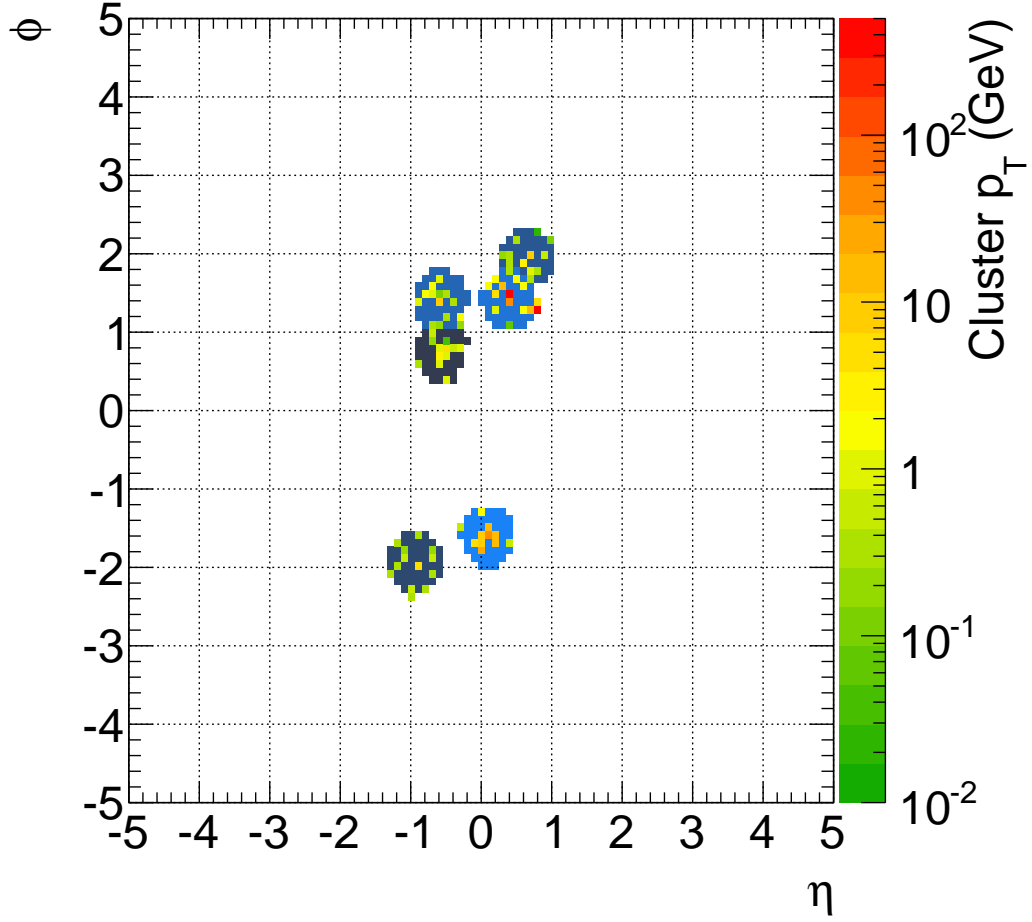This jet shape was designed to separate boosted hadronic objects, like

47

Figure 2.12: Event display of a merged b-jet in $(\eta, \phi) = (0.46, 1.41)$ and $p_T = 110$ GeV. The two b-hadrons are indicated as two red squares. The active area of the jet is shown in blue and the topoclusters belonging to the jet are shown in different colors, from green to orange, depending on their transverse momentum. The ΔR between the axes of the two k_t subjets in the jet is larger than 0.3. The two-subjet structure of the merged jet is displayed.

electroweak bosons and top quarks decaying into collimated showers of hadrons which a standard jet algorithm would reconstruct as single jets. A simple cut on the ratio τ_N/τ_{N-1} provides excellent discrimination power for N-prong hadronic objects[36] . In particular, τ_2/τ_1 can identify boosted W/Z and Higgs bosons, with the angular weighting exponent $\beta = 1$ providing the best discrimination.

The definition of N-subjettiness is not unique, and different choises can be used to give different weights to the emissions within a jet. The initial step of choosing candidate subjet axes is in fact unnecessary; the quantity in equation 2.4 can be minimised over the candidate subjet directions, further improving boosted object discrimination.

To avoid dependence on pile-up we consider track-based n-subjettiness, where the sum is over the tracks in the b-tagged jet. As seen for massive boosted objects, a jet with a two pronged structure, with all tracks clustered along two directions, is expected to have a smaller τ_2 value than a jet with a more uniform track distribution. The distributions of τ_2, shown in Fig. 2.13, display good separation between single and merged jets, but with the latter showing larger values than single. This behavior can be traced to the level of correlation between τ_2 and track-jet width, displayed in Fig. 2.14a, to be compared to the much lower correlation presented, for instance, between track-jet width and the jet track multiplicity, shown in Fig. 2.14b.

The correlation observed suggests to switch from an absolute to a width-normalized τ_2, and evaluate the ratio τ_2/τ_1. Fig. 2.15 thus shows the distributions for this observable. Somewhat larger values are obtained for single than for merged b-jets, specially at high p_T, however we decided not to use this variable as it offers only marginal discrimination.

Jet eccentricity In defining a jet moment there are several ways to weight
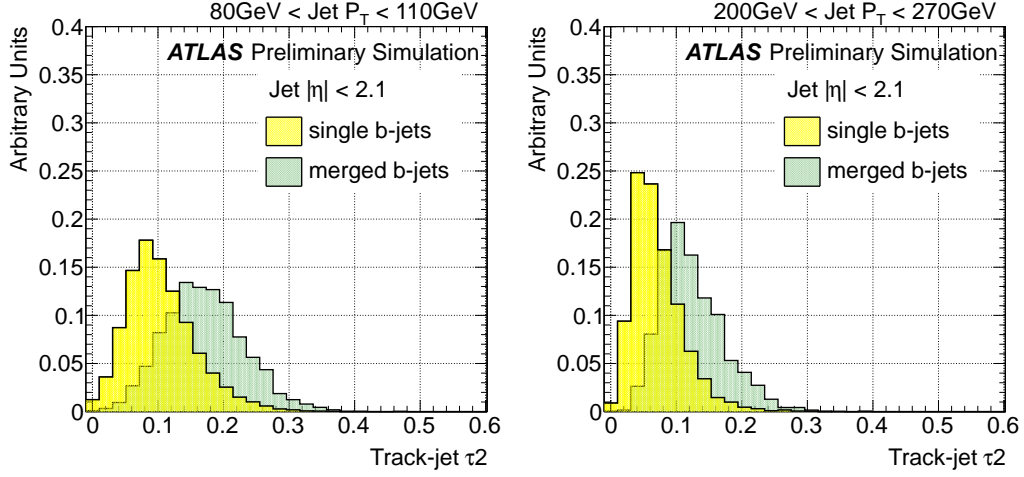
49

Figure 2.13: Distribution of τ_2 in jets for single and merged b-jets between 80 GeV to 110 GeV (left) and 200 GeV to 270 GeV (right).
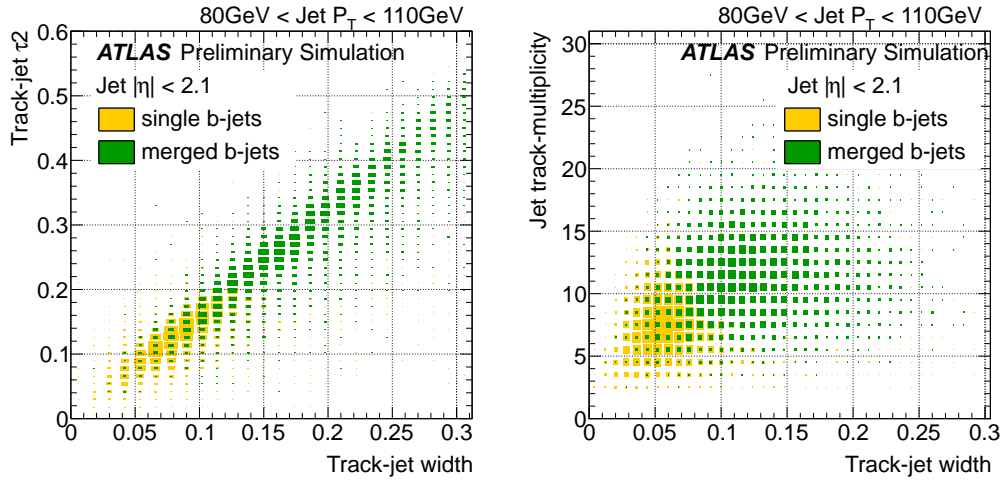

Figure 2.14: Correlation between τ_2 and track-jet width (left) and jet track multiplicity and track-jet width (right) for single and merged b-jets between 80 GeV to 110 GeV.
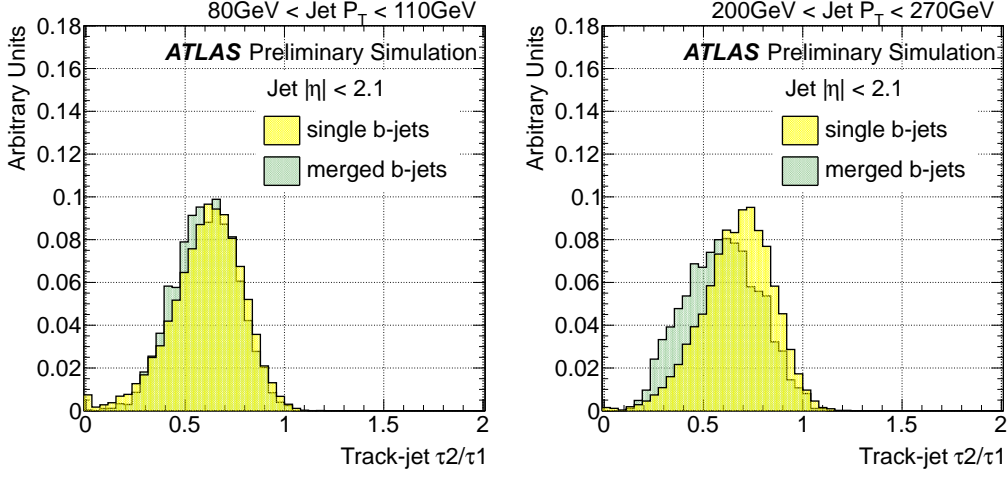
Figure 2.15: Distribution of τ_2/τ_1 in jets for single and merged b-jets between 80 GeV to 110 GeV (left) and 200 GeV to 270 GeV (right).

the momentum and define the center of the jet. We have defined the jet width as the first moment of the transverse energy with respect to the jet axis; another example of useful combination is the jet pull [38]. But it is also natural to look at higher moments, such as those contained in the 2×2 matrix,

$$\begin{bmatrix} \sum E_i \eta_i^2 & -\sum E_i \eta_i \phi_i \\ -\sum E_i \eta_i \phi_i & \sum E_i \phi_i^2 \end{bmatrix} \tag{2.5}$$

Here, (E_i, η_i, ϕ_i) are the jet constituent energy, pseudorapidity and azimuthal angle, respectively. The eigenvalues $\lambda_m \geq \lambda_p$ of this tensor are associated to the semiminor and semimajor axes of an elliptical jet, in the $\eta - \phi$ plane. The jet eccentricity, defined below, is a combination of these eigenvalues, and it is a measure of how elongated is the area of a jet,

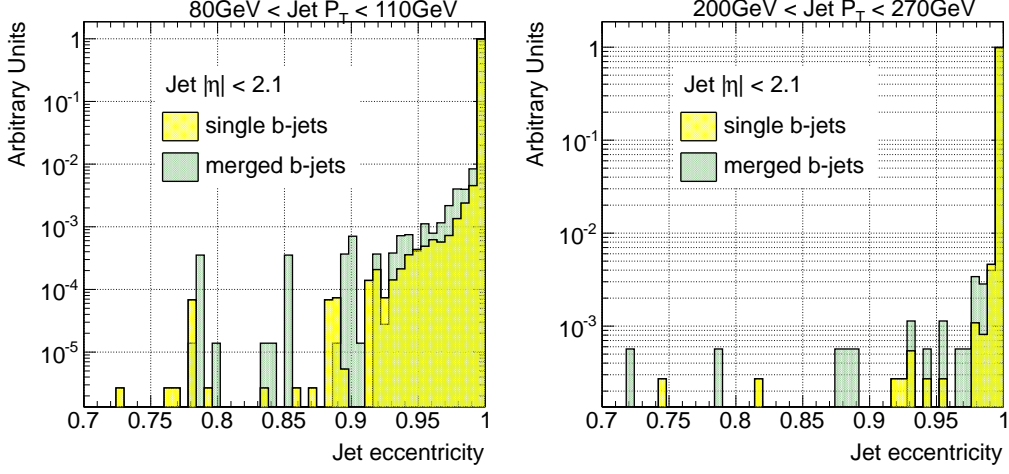$$e = \sqrt{1 - r^2} \tag{2.6}$$

Figure 2.16: Distribution of the jet eccentricity for single and merged b-jets between 80 GeV to 110 GeV (left) and 200 GeV to 270 GeV (right).

where the parameter r is defined as the ratio of the eigenvalues,

$$r = \frac{\lambda_m}{\lambda_p} = \frac{\sum E_i \eta_i^2 + \sum E_i \phi_i^2 - \sqrt{(\sum E_i \eta^2 - \sum E_i \phi_i^2)^2 + 4(\sum E_i \eta_i \phi_i)^2}}{\sum E_i \eta_i^2 + \sum E_i \phi_i^2 + \sqrt{(\sum E_i \eta^2 - \sum E_i \phi_i^2)^2 + 4(\sum E_i \eta_i \phi_i)^2}}.$$
(2.7)

Figure 2.16 shows the distribution of the jet eccentricity, built using track constituents. No significant difference in eccentricity was found between single and merged b-jets.

In order to better understand the behavior observed for this variable, further studies were performed using bigger cone jets to enhance the efficiency to capture the decay products in gluon to $b\bar{b}$-jets, in particular the anti-k_t 0.6 algorithm was used; and the ghost association procedure for cluster matching, for a calorimeter-based eccentricity. None of the above resulted in better single-merged separation.

2.3 Validation of the jet variables in data

In order to study the extent to which the simulation reproduces the distributions observed in data for the different variables explored a set of comparison plots is presented. Figures 2.17 and 2.18 show distributions of jet track multiplicity, track-jet width, ΔR between the axes of the two k_t subjets, $\max\{\Delta R(trk, trk)\}$ and τ_2 in two different p_T bins for b-tagged jets in di-jet Monte Carlo and data events passing selection described in Section 2.1.1. The distributions are normalized to unit area to allow for shape comparisons. There is a good agreement between data and simulation.

It should be remarked that the observed agreement is actually not a direct validation of the description in the MC of the relevant variables, but its convolution with the simulated relative fractions of light-, c-, b- and bb-jets in the b-tagged generated jet sample. To some extent, there could be some level of compensation between these two effects, although the agreement evaluated in b-jets selected with a looser cut of MV1 tagger as well as with another b-tagging algorithm is still ver good, suggesting that this compasation is not likely to occur in samples sufficiently enriched in b-jets.
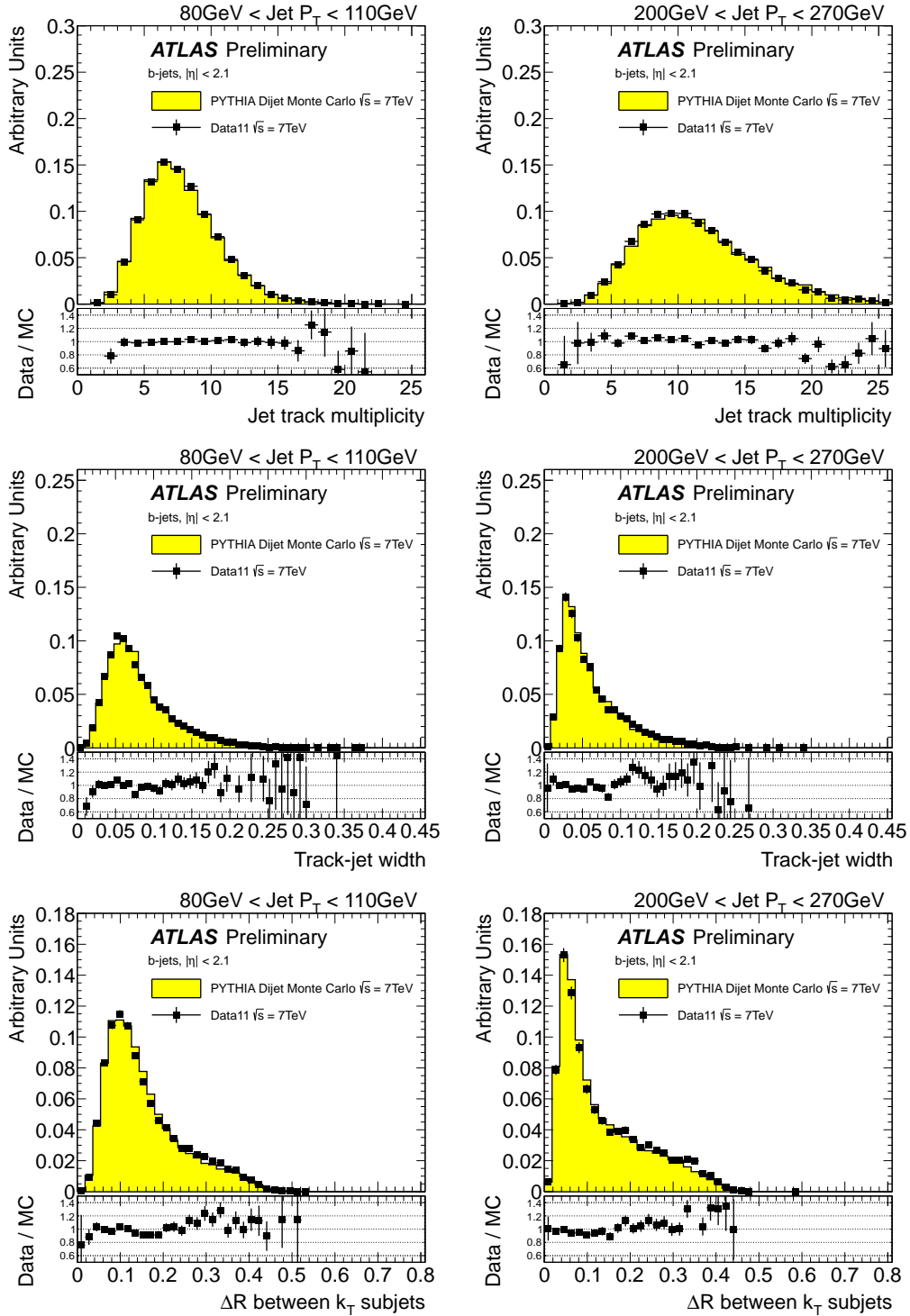
Figure 2.17: Distribution of three tracking variables in 2 different jet p_T bins, for experimental data collected by ATLAS during 2011 (solid black points), and simulated data (filled histograms). The ratio data over simulation is shown at the bottom of each plot.

54

Figure 2.18: Distribution of two tracking variables in two different jet p_T bins, for experimental data collected by ATLAS during 2011 (solid black points), and simulated data (filled histograms). The ratio data over simulation is shown at the bottom of each plot.
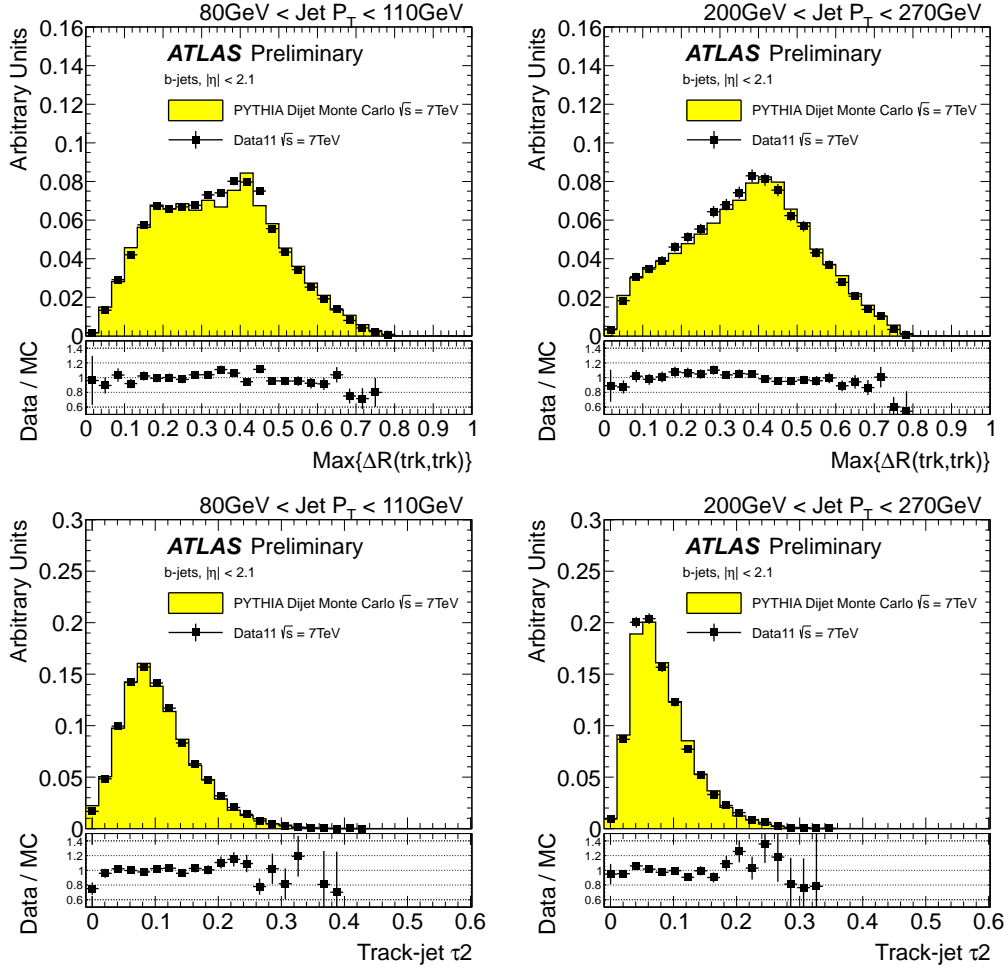
Bibliography

[1] ATLAS Collaboration.

[2] ATLAS Collaboration.

[3] W Lampl et al. Calorimeter Clustering Algorithms: Description and Performance. (ATL-LARG-PUB-2008-002. ATL-COM-LARG-2008-003), Apr 2008.

[4] M. Aharrouche et al. Energy linearity and resolution of the atlas electromagnetic barrel calorimeter in an electron test-beam. *Nuclear Instruments and Methods in Physics Research Section A: Accelerators, Spectrometers, Detectors and Associated Equipment*, 568(2):601 – 623, 2006.

[5] M Cooke, P S Mangeard, M Plamondon, M Aleksa, M Delmastro, L Fayard, S Henrot-VersillÃľ, F Hubaut, R Lafaye, W Lampl, J LÃľvÃłque, H Ma, E Monnier, J Parsons, P Pralavorio, Ph Schwemling, L Serin, B TrocmÃľ, G Unal, M Vincter, and H Wilkens. In situ commissioning of the ATLAS electromagnetic calorimeter with cosmic muons. *ATL-LARG-PUB-2007-013*, 2007.

[6] Georges Aad et al. Electron performance measurements with the ATLAS detector using the 2010 LHC proton-proton collision data. *Eur.Phys.J.*, C72:1909, 2012.

[7] ATLAS Collaboration.

[8] G. Abbiendi et al. Inclusive analysis of the b quark fragmentation function in Z decays at LEP. *Eur.Phys.J.*, C29:463–478, 2003.

[9] Koya Abe et al. Measurement of the b quark fragmentation function in Z0 decays. *Phys.Rev.*, D65:092006, 2002.

[10] Andy Buckley, Hendrik Hoeth, Heiko Lacker, Holger Schulz, and Jan Eike von Seggern. Systematic event generator tuning for the LHC. *Eur. Phys. J. C*, 65:331–357, 2010.

[11] M. G. Bowler. lt;igt;elt;/igt;lt;supgt;+lt;/supgt;lt;igt;elt;/igt;lt;supgt;âĹŠlt;/supgt; production of heavy quarks in the string model. *Zeitschrift fÃŒr Physik C Particles and Fields*, 11:169–174, 1981. 10.1007/BF01574001.

[12] T Cornelissen, M Elsing, S Fleischmann, W Liebig, E Moyse, and A Salzburger. Concepts, Design and Implementation of the ATLAS New Tracking (NEWT). *ATL-SOFT-PUB-2007-007. ATL-COM-SOFT-2007-002*, 2007.

[13] ATLAS Collaboration.

[14] J. Neyman and E. S. Pearson. On the Problem of the Most Efficient Tests of Statistical Hypotheses. *Royal Society of London Philosophical Transactions Series A*, 231:289–337, 1933.

[15] ATLAS Collaboration. Commissioning of the ATLAS high-performance b-tagging algorithms in the 7 TeV collision data. *ATLAS-CONF-2011-102*, 2011.

[16] ATLAS Collaboration. Performance of Impact Parameter-Based b-tagging Algorithms with the ATLAS Detector using Proton-Proton Collisions at $\sqrt{s} = 7$ TeV. *ATLAS-CONF-2010-091*, 2010.

[17] V Kostyukhin. Vkalvrt - package for vertex reconstruction in atlas. *ATL-PHYS-2003-031*, Aug 2003.

[18] ATLAS Collaboration. Performance of the ATLAS Secondary Vertex b-tagging Algorithm in 7 TeV Collision Data. *ATLAS-CONF-2010-042*, 2010.

[19] ATLAS Collaboration. Calibrating the b-Tag Efficiency and Mistag Rate in 35 pb^{-1} of Data with the ATLAS Detector. *ATLAS-CONF-2011-089*, 2011.

[20]

[21] ATLAS Collaboration.

[22] Torbjorn Sjostrand, Stephen Mrenna, and Peter Skands. PYTHIA 6.4 Physics and Manual. *JHEP*, 05:026, 2006.

[23] Atlas tunes of pythia 6 and pythia 8 for mc11. Technical Report ATL-PHYS-PUB-2011-009, CERN, Geneva, Jul 2011.

[24] Matteo Cacciari, Gavin P. Salam, and Gregory Soyez. The anti-k_t jet clustering algorithm. *JHEP*, 04:063, 2008.

[25] ATLAS Collaboration. Selection of jets produced in proton-proton collisions with the ATLAS detector using 2011 data. *ATLAS-CONF-2012-020*, 2012.

[26] Jason Gallicchio and Matthew D. Schwartz. Quark and gluon tagging at the lhc. *Phys. Rev. Lett.*, 107:172001, Oct 2011.

[27] ATLAS Collaboration. Light-quark and gluon jets in atlas. *ATLAS-CONF-2011-053*, 2011.

[28] D. Buskulic et al. Quark and gluon jet properties in symmetric three-jet events. *Physics Letters B*, 384(1âĂŞ4):353 – 364, 1996.

[29] Leandro G. Almeida, Seung J. Lee, Gilad Perez, Ilmo Sung, and Joseph Virzi. Top quark jets at the lhc. *Phys. Rev. D*, 79:074012, Apr 2009.

[30] R. Snihur. Subjet multiplicity in quark and gluon jets at d0. *Nuclear Physics B - Proceedings Supplements*, 79(1âĂŞ3):494 – 496, 1999. <ce:title>Proceedings of the 7th International Workshop on Deep Inelastic Scattering and QCD</ce:title>.

[31] Stephen D. Ellis and Davison E. Soper. Successive combination jet algorithm for hadron collisions. *Phys. Rev.*, D48:3160–3166, 1993.

[32] A. Abdesselam, E. Bergeaas Kuutmann, U. Bitenc, G. Brooijmans, J. Butterworth, et al. Boosted objects: A Probe of beyond the Standard Model physics. *Eur.Phys.J.*, C71:1661, 2011.

[33] Stephen D. Ellis, Christopher K. Vermilion, and Jonathan R. Walsh. Techniques for improved heavy particle searches with jet substructure. *Phys. Rev. D*, 80:051501, Sep 2009.

[34] Stephen D. Ellis and Davison E. Soper. Successive combination jet algorithm for hadron collisions. *Phys. Rev. D*, 48:3160–3166, Oct 1993.

[35] G.P. Salam M. Cacciari and Gregory Soyez. The Catchment Area of Jets. *JHEP*, 0804:42, 2008.

[36] Jesse Thaler and Ken Van Tilburg. Identifying Boosted Objects with N-subjettiness. *JHEP*, 1103:015:026, 2011.

[37] Iain W. Stewart, Frank J. Tackmann, and Wouter J. Waalewijn. n jettiness: An inclusive event shape to veto jets. *Phys. Rev. Lett.*, 105:092002, Aug 2010.

[38] Jason Gallicchio and Matthew D. Schwartz. Seeing in color: Jet superstructure. *Phys. Rev. Lett.*, 105:022001, Jul 2010.